 FDMP, vol.4, no.3, pp.139-161, 2008

Solutocapillary Convection in Spherical Shells with a Receding and Deforming Interface

Pravin Subramanian[1] **and Abdelfattah Zebib**[1]

Abstract: A theoretical and computational study of solutocapillary driven Marangoni instabilities in small spherical shells is presented. The shells contain a binary fluid with an evaporating solvent. The viscosity is a strong function of the solvent concentration, the inner surface of the shell is assumed impermeable and stress free, while non-linear boundary conditions are modeled and prescribed at the receding outer boundary. A time-dependent diffusive state is possible and may lose stability through the Marangoni mechanism due to surface tension dependence on solvent concentration (buoyant forces are negligible in this micro-scale problem). The Capillary number (Ca) provides a measure of the deviation from sphericity and to leading order in the limit $Ca \to 0$ the outer surface evolves with time in a convective state as it does in the diffusive state. We model the motion in this limit and compute supercritical, nonlinear, time-dependent, axisymmetric and three-dimensional, infinite Schmidt number solutocapillary convection. The normal stress balance imposes compatibility restrictions and allows two admissible states: axisymmetric hemispherical convection and three-dimensional solutions exhibiting cubic symmetry. We employ global mass conservation to compute upper bounds on the companion $O(Ca)$ free surface deformations.

1 Introduction

It is well known that surface tension dominates buoyant forces either in small scale hydrodynamics or in a microgravity environment. A temperature difference across a thin fluid layer can thus drive convective instabilities due to surface tension variation with temperature (Pearson 1958; Smith 1966). Likewise these Marangoni instabilities can arise in a binary fluid contained in a spherical shell due to surface tension variation with either temperature or concentration (Cloot and Lebon 1985; Hoefsloot et al 1990; Wilson 1994). This latter problem gained interest in recent times in the context of manufacturing small poly (α-methyl styrene) spherical shells by microencapsulation, used as laser targets in inertial confinement fusion (McQuillan 1997). Almost perfect target sphericity is required in order to eliminate Rayleigh-Taylor instabilities during implosion. However it was experimentally hypothesized that this smoothness can be defeated by Marangoni instabilities driven by surface tension dependence on the evaporating solvent concentration (McQuillan and Greenwood 1999; McQuillan and Takagi 2002). Linear stability of the underlying time dependent diffusive state (Subramanian et al 2005a) demonstrated that this indeed may be the case.

The theoretical model (Subramanian et al 2005a) considered a solute and a solvent binary fluid in a spherical shell. The solvent evaporates in an aqueous environment with a prescribed mass transfer coefficient while the viscosity grows exponentially as the solvent depletes. The inner surface was assumed impermeable and stress free. The Capillary number Ca was taken small so that deformations of the receding outer surface were also small $O(Ca)$. Linear stability limits, found independent of the azimuthal wavenumber, were established both through a frozen-time, quasi-steady state approximation, as well as by integrating the initial value problem in time subject to arbitrary initial conditions. It was shown that in the limit $Ca \to 0$ the normal stress balance re-

[1] Mechanical & Aerospace Engineering, Rutgers University, Piscataway, NJ, 08854

quired the outer surface to recede as it does in the diffusive state. This enabled computations of nonlinear axisymmetric supercritical convection (Subramanian et al 2005b) that were consistent with linear predictions. A pair of axisymmetric states, one of them hemispherically symmetric, were found. The nonlinear problem is thus degenerate with additional three dimensional states possible.

In the present study we reconsider the previous model (Subramanian et al 2005a; Subramanian et al 2005b). The normal stress balance is employed to both decrease the degeneracy and to determine the magnitude of surface deformation. In section 2 we present the full nonlinear problem and boundary conditions at the impermeable and stress free inner boundary and the receding outer surface. In sections 3 and 4 we compute nonlinear, time-dependent, infinite Schmidt number, axisymmetric (Subramanian et al 2005b) and three-dimensional convection at parameter values which mimic the experiments (McQuillan and Greenwood 1999; McQuillan and Takagi 2002). Detailed analysis of the normal stress boundary condition at the receding interface and derivation of the solvability condition are given in section 5 and Appendices A, B and C. Global mass conservation is then utilized to calculate an upper bound on the $O(Ca)$ surface deformations associated with compatible solutions.

2 Theory and Mathematical Model

Consider the spherical shell shown in Figure 1 of initial thickness $L_r = R^*_{2_0} - R^*_1$, where R^*_1 and $R^*_{2_0}$ are the shell's inner and initial outer radii respectively. The center of the shell is assumed fixed and possible Marangoni-migration phenomena is neglected. The aspect ratio of the shell is $\eta = R^*_1/R^*_{2_0} < 1$ (all starred quantities are dimensional). The shell contains a mixture of solvent and solute with mass concentrations C^* and $(1 - C^*)$, respectively. The ambient is a mixture of solvent and water into which the solvent in the shell is evaporating. Thus there is a net mass flux across the receding outer interface.

The physical quantities are non-dimensionalized with respect to the scales ρ_r, μ_r, ν_r, D_r, L_r, $t_r = L_r{}^2/D_r$, C_r, D_r/L_r, μ_r/t_r for density, dynamic viscosity, kinematic viscosity, mass diffusivity, length, time, concentration, velocity, and pressure, respectively. We assume linear variation of interfacial tension σ^* with concentration C^* according to:

$$\sigma^* = \sigma_r - \gamma(C^* - C_r) \tag{1}$$

where subscript r designates a reference state and $\gamma = -d\sigma^*/dC^*$ which is taken small and positive. The Capillary number is defined as:

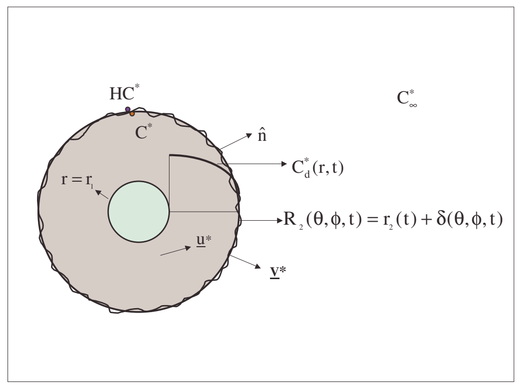

Figure 1: Sketch of the mathematical model

$$Ca = \Delta\sigma/\overline{\sigma} = (\overline{\sigma} - \sigma_r)/\overline{\sigma} = \gamma C_r/\overline{\sigma} \tag{2}$$

where $\overline{\sigma} = \sigma_r + \gamma C_r$ is a typical value of the surface tension. Other relevant non-dimensional quantities are: the mass transfer Biot number $Bi = KL_r/\rho_r D_r$ based on a mass transfer coefficient K assumed constant, the Reynolds number $Re = \gamma C_r L_r/\mu_r \nu_r$ and the Marangoni number $Ma = Re \cdot Sc$, where the Schmidt number $Sc = \nu_r/D_r$. We assume constant density and mass diffusivity at their reference values and $\mu(C)$ is a prescribed function $\mu(C) = e^{\alpha(1-C)}$, where $\alpha = 25.675C_r$ for the PAMS-FB system. C_∞ is the concentration of the solvent in the ambient and H is a partition coefficient (thermodynamic property) relating the equilibrium concentration of the solvent in the shells to its concentration in the ambient water. To compare with the experiments (McQuillan and Greenwood 1999; McQuillan and Takagi 2002) we take C_∞ in the range $0.0001-0.0014$ which is close to saturation, Bi in the range $1-5$, and $H=0.0015$. Because the viscosity of the PAMS-FB is much larger than that of the water in the core, and because in the experiments the mass transfer coefficient at the inner surface is much smaller than that at outer surface, it will be assumed here that the inner surface is impermeable and stress free (Subramanian et al 2005a) . The value of the diffusion coefficient which sets the time scale is not precisely known for our system and is assumed $1.8\times10^{-6}cm^2/s$ (Subramanian et al 2005a).

The motion is described in a spherical coordinate system (r,θ,ϕ). The $O(1)$ dimensionless system of the governing equations written in the standard divergence form suitable for solution by the finite volume method (Patankar 1980), and boundary conditions (Subramanian et al 2005a) for nonlinear variable viscosity, infinite Sc, and three-dimensional convection are:

$$\frac{1}{r^2}\frac{\partial}{\partial r}(r^2U_r)+\frac{1}{rsin\theta}\frac{\partial}{\partial\theta}(sin\theta U_\theta)+\frac{1}{rsin\theta}\frac{\partial}{\partial\phi}(U_\phi)=0 \quad (3)$$

$$\begin{aligned}0=&-\frac{\partial p}{\partial r}+\frac{1}{r^2}\frac{\partial}{\partial r}\left[2\mu r^2\frac{\partial U_r}{\partial r}\right]\\&+\frac{1}{r^2sin\theta}\frac{\partial}{\partial\theta}\left[\mu sin\theta\frac{\partial U_r}{\partial\theta}\right]+\frac{1}{r^2sin^2\theta}\frac{\partial}{\partial\phi}\left[\mu\frac{\partial U_r}{\partial\phi}\right]\\&-\frac{4\mu U_r}{r^2}+\frac{\partial\mu}{\partial\theta}\left[\frac{-U_\theta}{r^2}+\frac{1}{r}\frac{\partial U_\theta}{\partial r}\right]\\&+\frac{1}{sin\theta}\frac{\partial\mu}{\partial\phi}\left[\frac{-U_\phi}{r^2}+\frac{1}{r}\frac{\partial U_\phi}{\partial r}\right]\\&+\mu\Big[-\frac{3}{r^2}\frac{\partial U_\theta}{\partial\theta}-\frac{3}{r^2sin\theta}\frac{\partial U_\phi}{\partial\phi}+\frac{cot\theta}{r}\frac{\partial U_\theta}{\partial r}\\&\quad-\frac{3cot\theta U_\theta}{r^2}+\frac{1}{r}\frac{\partial^2U_\theta}{\partial r\partial\theta}+\frac{1}{rsin\theta}\frac{\partial^2U_\phi}{\partial r\partial\phi}\Big] \quad (4)\end{aligned}$$

$$\begin{aligned}0=&-\frac{1}{r}\frac{\partial p}{\partial\theta}+\frac{1}{r^2}\frac{\partial}{\partial r}\left[\mu r^2\frac{\partial U_\theta}{\partial r}\right]\\&+\frac{1}{r^2sin\theta}\frac{\partial}{\partial\theta}\left[2\mu sin\theta\frac{\partial U_\theta}{\partial\theta}\right]\\&+\frac{1}{r^2sin^2\theta}\frac{\partial}{\partial\phi}\left[\mu\frac{\partial U_\theta}{\partial\phi}\right]-\frac{2\mu U_\theta[cot^2\theta+1]}{r^2}\\&+\frac{\partial\mu}{\partial r}\left[\frac{-U_\theta}{r}+\frac{1}{r}\frac{\partial U_r}{\partial\theta}\right]+\frac{\partial\mu}{\partial\theta}\left[\frac{2U_r}{r^2}\right]\\&+\frac{\partial\mu}{\partial\phi}\left[\frac{1}{r^2sin\theta}\frac{\partial U_\phi}{\partial\theta}-\frac{cot\theta U_\phi}{r^2sin\theta}\right]\\&+\mu\Big[\frac{4}{r^2}\frac{\partial U_r}{\partial\theta}-\frac{3cot\theta}{r^2sin\theta}\frac{\partial U_\phi}{\partial\phi}\\&\quad+\frac{1}{r}\frac{\partial^2U_r}{\partial r\partial\theta}+\frac{1}{r^2sin\theta}\frac{\partial^2U_\phi}{\partial\theta\partial\phi}\Big] \quad (5)\end{aligned}$$

$$\begin{aligned}0=&-\frac{1}{rsin\theta}\frac{\partial p}{\partial\phi}+\frac{1}{r^2}\frac{\partial}{\partial r}\left[\mu r^2\frac{\partial U_\phi}{\partial r}\right]\\&+\frac{1}{r^2sin\theta}\frac{\partial}{\partial\theta}\left[\mu sin\theta\frac{\partial U_\phi}{\partial\theta}\right]\\&+\frac{1}{r^2sin^2\theta}\frac{\partial}{\partial\phi}\left[2\mu\frac{\partial U_\phi}{\partial\phi}\right]\\&-\frac{\mu U_\phi[cot^2\theta+1]}{r^2}+\frac{\partial\mu}{\partial r}\left[\frac{-U_\phi}{r}+\frac{1}{rsin\theta}\frac{\partial U_r}{\partial\phi}\right]\\&+\frac{\partial\mu}{\partial\theta}\left[-\frac{cot\theta U_\phi}{r^2}+\frac{1}{r^2sin\theta}\frac{\partial U_\theta}{\partial\phi}\right]\\&+\frac{\partial\mu}{\partial\phi}\left[\frac{2cot\theta U_\theta}{r^2sin\theta}+\frac{2U_r}{r^2sin\theta}\right]\\&+\mu\Big[\frac{4}{r^2sin\theta}\frac{\partial U_r}{\partial\phi}+\frac{3cot\theta}{r^2sin\theta}\frac{\partial U_\theta}{\partial\phi}\\&\quad+\frac{1}{rsin\theta}\frac{\partial^2U_r}{\partial r\partial\phi}+\frac{1}{r^2sin\theta}\frac{\partial^2U_\theta}{\partial\theta\partial\phi}\Big] \quad (6)\end{aligned}$$

$$\begin{aligned}&\frac{\partial C}{\partial t}+\frac{1}{r^2}\frac{\partial}{\partial r}(r^2U_rC)+\frac{1}{rsin\theta}\frac{\partial}{\partial\theta}(sin\theta U_\theta C)\\&+\frac{1}{rsin\theta}\frac{\partial}{\partial\phi}(U_\phi C)=\\&\frac{1}{r^2}\frac{\partial}{\partial r}(r^2\frac{\partial C}{\partial r})+\frac{1}{r^2sin\theta}\frac{\partial}{\partial\theta}(sin\theta\frac{\partial C}{\partial\theta})\\&\quad+\frac{1}{r^2sin^2\theta}(\frac{\partial^2C}{\partial\phi^2}) \quad (7)\end{aligned}$$

with the boundary conditions at $r=r_1$ given by:

$$U_r=\frac{\partial}{\partial r}\left(\frac{U_\theta}{r}\right)=\frac{\partial}{\partial r}\left(\frac{U_\phi}{r}\right)=\frac{\partial C}{\partial r}=0 \quad (8)$$

and at the receding outer boundary $r=r_{2d}(t)$ determined from the diffusive state solution (Subramanian et al 2005a), we have:

$$U_r=BiC_r(HC-C_\infty)+\dot{r_{2d}} \quad (9)$$

$$\frac{\partial C}{\partial r}=-Bi(HC-C_\infty)(1-CC_r) \quad (10)$$

$$\mu\left[r\frac{\partial}{\partial r}\left(\frac{U_\theta}{r}\right)+\frac{1}{r}\frac{\partial}{\partial\theta}(U_r)\right]=-\frac{Ma}{r}\frac{\partial C}{\partial\theta} \tag{11}$$

$$\mu\left[r\frac{\partial}{\partial r}\left(\frac{U_\phi}{r}\right)+\frac{1}{rsin\theta}\frac{\partial}{\partial\phi}(U_r)\right]=-\frac{Ma}{rsin\theta}\frac{\partial C}{\partial\phi} \tag{12}$$

The inertia terms in the momentum equations have been neglected as they multiply $1/Sc \simeq 10^{-6}$. The appropriate boundary conditions imposed in the θ and ϕ directions are discussed in detail in the following sections.

The normal stress balance at the receding outer interface is used to compute the magnitude of surface deflection and hence the deviation from sphericity; it is given by:

$$\hat{n}\cdot S\cdot\hat{n}=-\frac{Ma}{Ca}(1-CaC)\nabla\cdot\hat{n} \tag{13}$$

where $S=-pI+\tau$ is the stress tensor in the fluid (I is the unit tensor and $\tau=\mu(\nabla\underline{u}+{}^t\nabla\underline{u})$ is the viscous stress tensor). $\hat{n}$ is the outward pointing normal at the receding outer boundary given by:

$$\hat{n}=\frac{\nabla F}{|\nabla F|}=\frac{(1,-\frac{1}{r}\partial_\theta R_2,-\frac{1}{rsin\theta}\partial_\phi R_2)}{\left(1+(\frac{1}{r}\partial_\theta R_2)^2+(\frac{1}{rsin\theta}\partial_\phi R_2)^2\right)^{1/2}} \tag{14}$$

where $F(\underline{x},t)=r-R_2(\theta,\phi,t)=0$ is the location of the perturbed outer boundary. Hence the normal stress balance at the outer interface $r=r_{2d}(t)$ reduces to (see Appendix A):

$$-\left[p\frac{r_{2d}^2}{Ma}-\frac{2r_{2d}}{Ca}\right]+2\mu\frac{r_{2d}^2}{Ma}\frac{\partial u_r}{\partial r}|_{r=r_{2d}}-2Cr_{2d} = [2-L^2]\left(\frac{\delta}{Ca}\right)+O(\delta) \tag{15}$$

Here the operator:

$$L^2=-\left(\frac{1}{sin\theta}\frac{\partial}{\partial\theta}sin\theta\frac{\partial}{\partial\theta}+\frac{1}{sin^2\theta}\frac{\partial^2}{\partial\phi^2}\right) \tag{16}$$

is the negative of the surface Laplacian on a unit sphere.

3 Axisymmetric Convection

The system of equations and boundary conditions for axisymmetric convection are derived from the governing three-dimensional equations by eliminating the dependence in the ϕ direction. In the full sphere axisymmetric model, we also impose the following symmetry boundary conditions at $\theta=0$ and π:

$$U_\theta=\frac{\partial U_r}{\partial\theta}=\frac{\partial C}{\partial\theta}=0 \tag{17}$$

which yields convection with even and odd number of cells that correspond to the degree of surface harmonic l (employed in the linear theory (Subramanian et al 2005a)). The hemispherical model with the symmetry conditions (17) imposed at $\theta=0$ and $\pi/2$ results (Subramanian et al 2005b) in convection with even number of cells and is further investigated here.

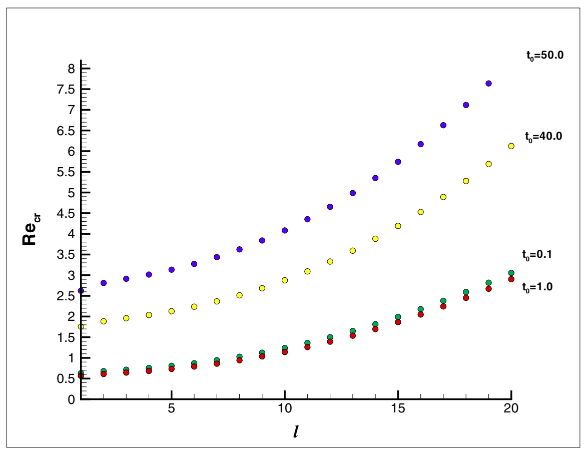

Figure 2: Variation (Subramanian et al 2005a) of Re_{cr} with wavenumber l for the 1 mm shells (inner radius = 0.470 mm and the initial outer radius = 0.592 mm) at various frozen times t_0. Concentration, time and length scales are respectively, 0.92, 83 sec and 0.122 mm, $Bi=5$ and $C_\infty=0.0001$.

3.1 Numerical Scheme

A front-fixing coordinate transformation given by $\zeta=(r-r_1)/(r_2(t)-r_1)$ is employed where $0\leq\zeta\leq 1$ for the shells at all times (t). The transformed equations in the computational domain (ζ,θ,t) are rigorously derived (not shown here) and the partial differential equations expressed in the divergence form are discretized via a second-order accurate finite volume method. The computational domain is divided into a number of cells whose surfaces coincide with the spherical coordinate surfaces. The grid points are located at the geometric centers of these small cells and additional boundary points are included to incorporate the boundary conditions. The equations are integrated over each small control volume assuming linear interpolation.

The primitive variable formulation used calculates the pressure and concentration at the volume centers (grid points) while the velocities are staggered at the volume faces to avoid unrealistic pressure fields and associated numerical instabilities. The viscosity which is a function of the concentration is also calculated at the grid points. The average values for μ and its derivatives at cell interfaces are found by either linear or harmonic interpolations. Time marching is accomplished by either a fully implicit first-order forward Euler scheme or by a second-order accurate Crank-Nicholson scheme, and an iterative approach (based on the SIMPLER algorithm (Patankar 1980)) is used. Numerical convergence studies were performed using the solution obtained from the finest discretization in space and time as the reference. By changing the values of grid spacing in the r and θ directions, along with the time step the solutions were compared to the reference solution. The results reported here are with a 51×51 grid and a time step 0.01. Under-relaxation was employed to obtain convergence of the iterative solution of the nonlinear equations. Computations are performed and supercritical patterns are investigated in the relevant parameters space with random initial conditions.

3.2 *Numerical Results*

The maximum growth rates of perturbations (σ_{max}) determined by solving the linear eigenvalue problem and/or initial value problem subject to random initial conditions revealed that modes with increasing l are preferred at later times (Subramanian et al 2005a; Subramanian 2005). In this section, we present results for nonlinear axisymmetric convection in terms of the stream function (Ψ) and concentration (C) contours.

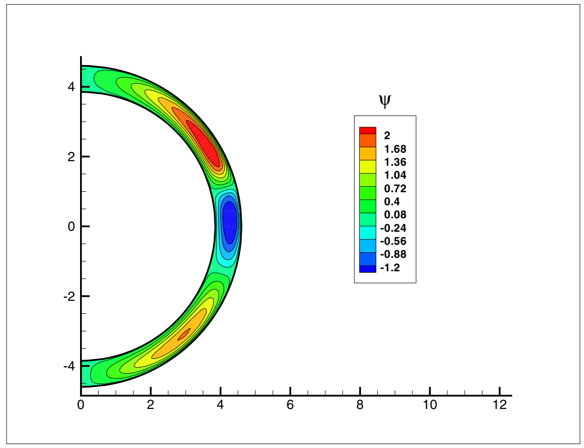

Figure 5: Similar to Figure 3a at time t=40.0

1 mm Shells

The critical curves (Subramanian et al 2005a) for the 1 mm shells at the parameter values of Figure 2 show that at all times during the curing process Re_{cr} always corresponds to mode 1. Since the initial state is one of uniform concentration, Re_{cr} first decreases with time as a destabilizing gradient develops and then increases with viscosity increase due to loss of solvent.

We compute nonlinear axisymmetric convection in the 1 mm shells for this set of parameters which mimic the experiments and an operating Reynolds number Re_{op}=2.0. According to Figure 2 this value of Re_{op} is supercritical during early times while subcritical at later times. Thus we expect convection to first grow and to gradually weaken at later times. Our nonlinear calculations are consistent with this prediction as can be seen in Figure 3a where a one cell motion ($l = 1$) appears at early times and develops into multiple cell convection at later times. As seen in Figure 3b the concentration C contour plot corresponding to Figure 3a [both plotted in the physical domain (r, θ)] shows that at early times the variation of C in the shells is almost diffusive since the motion is very weak as indicated by the values of Ψ in Figure 3a. A five cell motion ($l = 5$) appears at a later time $t = 15.0$ and is presented

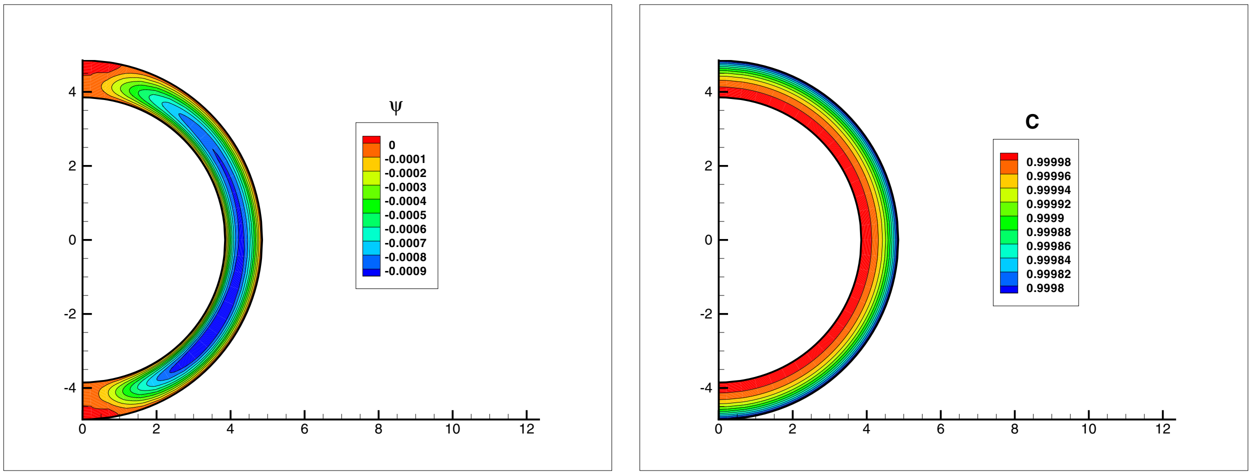

(a) (b)

Figure 3: (a) Full sphere axisymmetric convection stream function (Ψ) for 1 mm shells in the physical domain (r,θ) at time t=0.1 and Re_{op}=2.0, at parameter values of Figure 2. (Negative values of Ψ indicate counter-clockwise motion) (b) Corresponding concentration (C) contour plot in the physical domain.

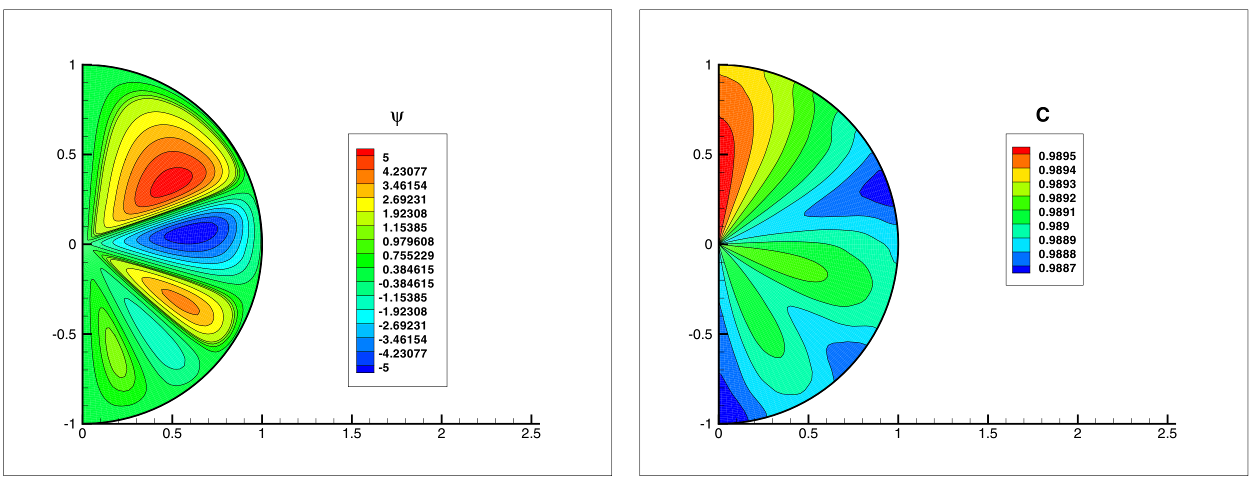

(a) (b)

Figure 4: Similar to Figure 3 but in the computational domain (ζ,θ) at time t=15.0

in the computational domain (ζ,θ) in Figure 4a. As can be seen in the C contour plot in Figure 4b the contours are shifted in the direction of motion, with upwelling at the north pole and downwelling at the south pole. The contours in the remaining parts of the shell are shifted due to the multiple cell motion. The motion changes to the three cell convective pattern at $t = 40.0$ shown in Figure 5. The corresponding plot in the (ζ,θ) domain is presented in Figure 6a for clarity. This initial increase in l followed by a decrease in l as time progresses is in agreement with the σ_{max} calculated in the linear theory because Re_{op} is largely supercritical at early times, while the difference between Re_{op} and Re_{cr} decreases as time progresses. At later times the strength of the circulation as measured by Ψ_{max} diminishes as the Re_{op} is subcritical and the motion dies out eventually. It should be noted that the computed cellular patterns are in good agreement with the critical curves of Figure 2 which are almost flat up to modes 3-5 at early times. As can be seen from Figure 3a and 5, the

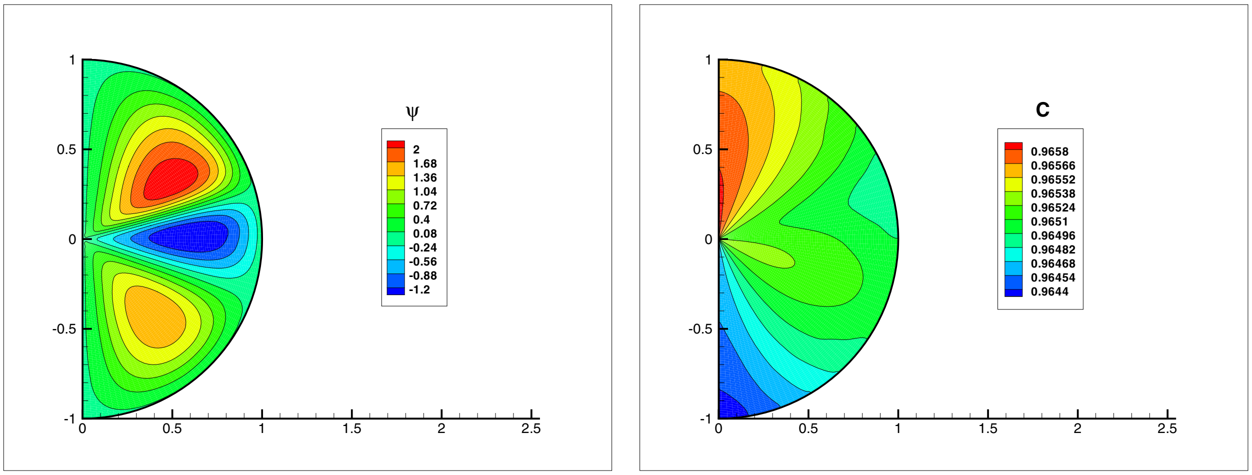

(a) (b)

Figure 6: (a) Full sphere convection Ψ in the computational domain (ζ, θ) of Figure 5. (b) Corresponding concentration (C) contour plot.

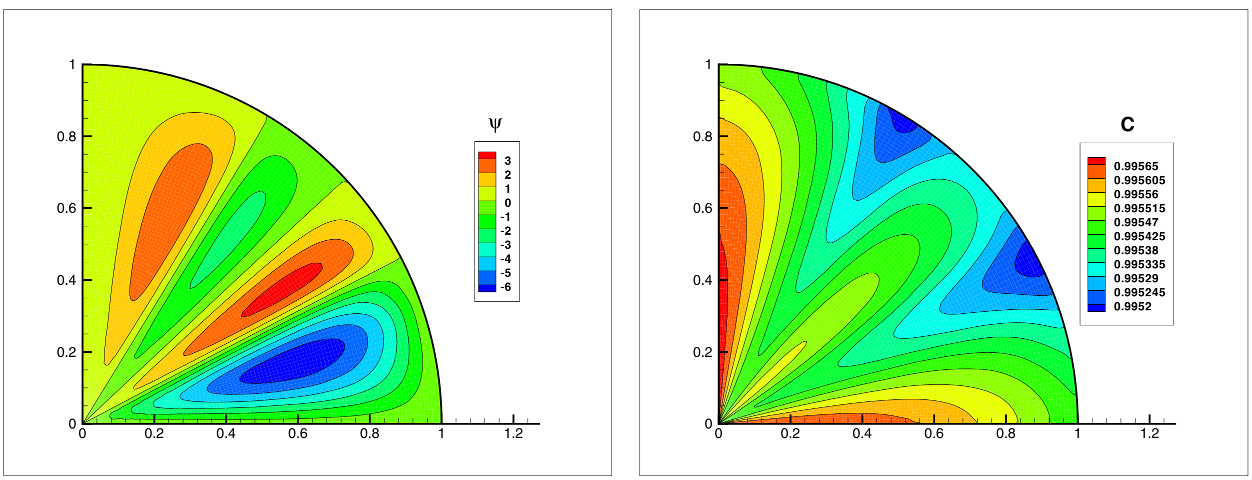

(a) (b)

Figure 7: (a) Hemispherical axisymmetric convection Ψ for 1 mm shells in the (ζ, θ) domain at time t=5.0 and Re_{op}=2.0, at parameter values of Figure 2. (b) Corresponding concentration (C) contour plot.

thickness of the shell in the physical domain decreases as time progresses since the outer radius recedes due to the evaporation of the solvent.

Figure 6b gives the corresponding concentration (C) field of the motion in Figure 6a with the iso-concentration lines pushed in the direction of motion. Hemispherical axisymmetric convection is also possible as shown in Figures 7 and 8 where an eight cell motion ($l = 8$) appears at an early time $t = 5.0$ and evolves into a four cell ($l = 4$) motion at $t = 20.0$.

2 mm Shells

The critical curves in Figure 9 show that at early times, Re_{cr} corresponds to mode 2, while higher modes are preferred at later times.

For $Re_{op} = 2.0$ which is supercritical at early times, multiple cell motions develop up to $t = 300.0$. Figures 10 and 11a show a nine cell motion ($l = 9$) at time $t = 200.0$ from the full sphere calculations. This is consistent with the critical curves (Figure 9) that are almost flat up to mode

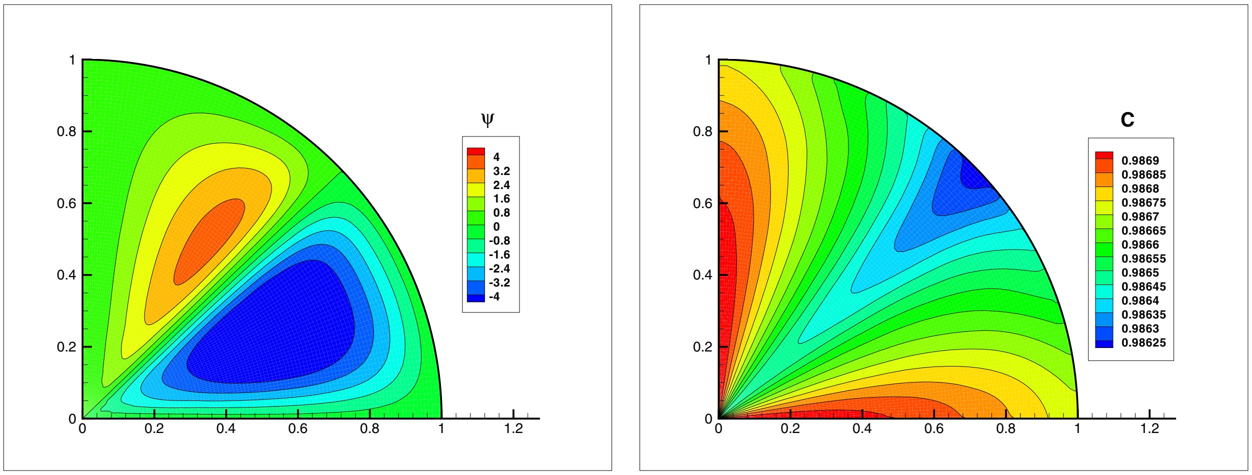

(a) (b)

Figure 8: (a) Hemispherical axisymmetric convection Ψ for 1 mm shells in the (ζ, θ) domain at time t=20.0 and Re_{op}=2.0, at parameter values of Figure 2. (b) Corresponding concentration (C) contour plot.

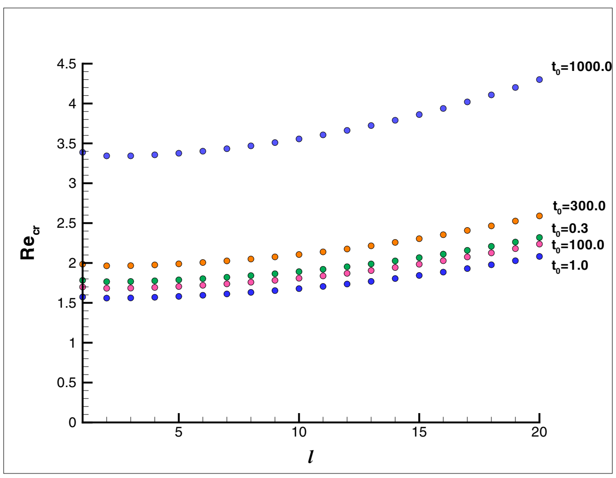

Figure 9: Variation (Subramanian et al 2005a) of Re_{cr} with wavenumber l for the 2 mm shells (inner radius = 1.000 mm and the initial outer radius = 1.077 mm) at various frozen times t_0. Concentration, time and length scales are respectively, 0.82, 33 sec and 0.077 mm, $Bi = 1$ and $C_\infty = 0.0014$.

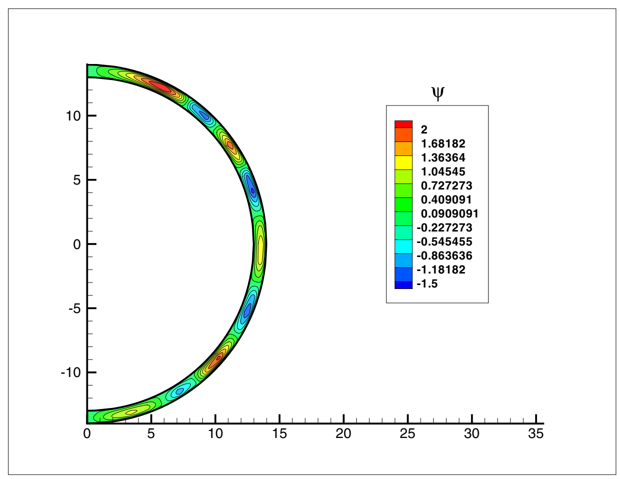

Figure 10: Full sphere axisymmetric convection stream function Ψ for 2 mm shells in the physical domain (r, θ) at time t=200.0 and Re_{op}=2.0, at parameter values of Figure 9.

8-10 with multiple modes excited and interacting nonlinearly. Due to upwelling at one pole and downwelling at the other, the C contours are shifted upwards as can be seen from Figure 11b. One also notes the shifts in the C contours in the remaining parts of the shell due to the multiple cell motions. As expected, at later times when the Re_{op} is subcritical, the convection slowly dies down as two cell motions until there is no further motion in the shells.

Finally, Figure 12a shows the hemispherical axisymmetric solution with a four cell motion ($l = 4$) at time $t = 300.0$ and the corresponding C contour plot is shown in Figure 12b.

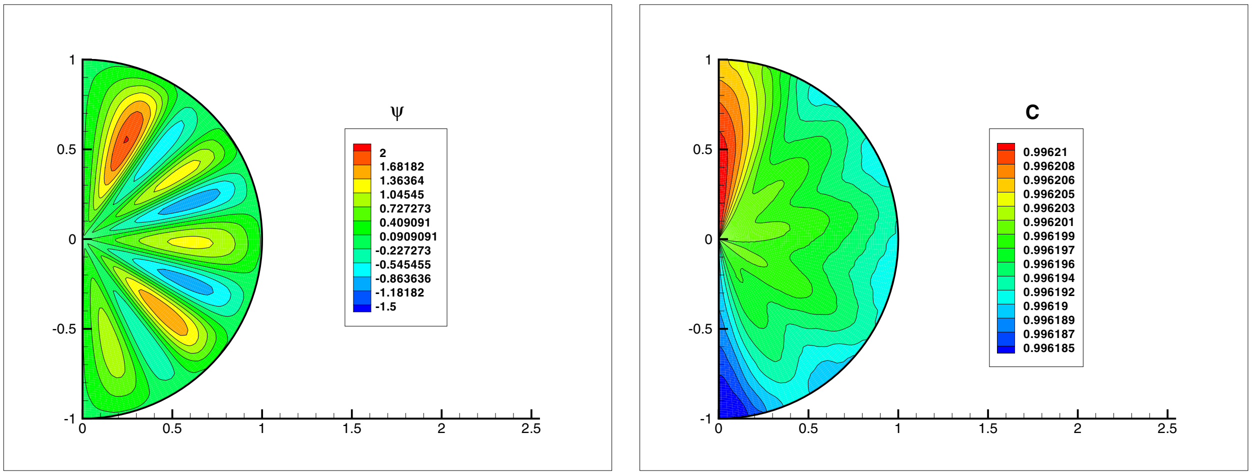

(a) (b)

Figure 11: (a) Full sphere axisymmetric convection Ψ in the computational domain (ζ, θ) corresponding to Figure 10. (b) Corresponding concentration (C) contour plot.

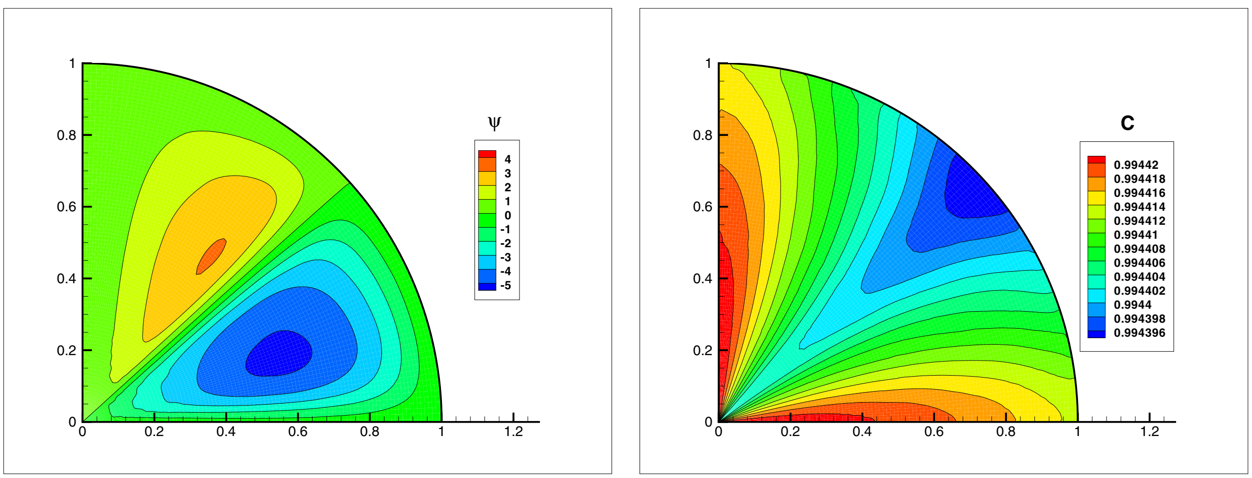

(a) (b)

Figure 12: (a) Hemispherical axisymmetric convection stream function Ψ for 2 mm shells in the (ζ, θ) domain at time t=300.0 and Re_{op}=2.0, at parameter values of Figure 9. (b) Corresponding concentration (C) contour plot.

4 Three-Dimensional Convection

The solutions to the governing 3D system of equations (3)-(12) are required to be finite at $\theta = 0\&\pi$ and 2π periodic in ϕ. 3D hemispherical convection is also possible with symmetry conditions imposed at $\theta = \pi/2$:

$$U_\theta = \frac{\partial U_r}{\partial \theta} = \frac{\partial U_\phi}{\partial \theta} = \frac{\partial C}{\partial \theta} = 0 \qquad (18)$$

Convection with tetrahedral symmetry is also possible and satisfies the following symmetry boundary conditions at $\phi = 0$ and $\phi = \pi$:

$$U_\phi = \frac{\partial U_r}{\partial \phi} = \frac{\partial U_\theta}{\partial \phi} = \frac{\partial C}{\partial \phi} = 0 \qquad (19)$$

Convection with cubic symmetry exhibits both symmetries given by (18) and (19) in addition to symmetry about $\phi = \pi/2$. Thus there are four possible 3D solutions: full sphere convection, or convection with hemispherical, tetrahedral, or cubic symmetries. It was a remarkable finding that starting from arbitrary initial conditions convection always evolved into the cubic pattern. It should be noted that these symmetries are possible in our small capillary number model. If large surface deformations are considered there will exist flow states with all the symmetries broken.

4.1 Numerical Scheme

As in the case of axisymmetric convection, we employ the front-fixing coordinate transformation given by $\zeta = (r - r_1)/(r_2(t) - r_1)$ where $0 \leq \zeta \leq 1$ for the shells at all times (t). The transformed equations in the computational domain (ζ, θ, ϕ, t) are derived and nonlinear three-dimensional convection is computed using the second-order accurate finite volume approach. Time marching is accomplished by either a fully implicit first-order forward Euler scheme or by a second-order accurate Crank-Nicholson scheme.

Since an orthogonal grid in spherical coordinates is used, the convergence of lines of longitude at the poles results in grid points being much more closely spaced in the polar regions. This "pole problem" can sometimes lead to spurious results near the coordinate singularities at the poles. The staggered, control volume discretization handles the singularities for all but latitudinal velocity U_θ by defining the polar control volumes to be of zero size. Zero size control volumes have no mass, momentum, or species fluxes into or out of the volume; they do not contribute to the final solution, and thus we need not compute the dependent variables at the poles. The grid staggering, however, results in half sized control volumes at the pole for the latitudinal component of the momentum equation. This requires a solution for U_θ at the poles. To mitigate this situation, the control volumes adjacent to the polar control volumes are expanded to include the regions that would make up for the half size control volumes. Tests of the effect of this treatment at the polar region were performed wherein converged solutions with cubic symmetry (which have upwelling at the pole) were rotated in the θ direction, randomly perturbed, and fed back into the numerical model as initial conditions. These rotated patterns rapidly converged to new solutions, which maintained the shifted orientation and had fluid flow and mass transfer properties identical to the original, unrotated solutions. In another test, the solutions of the numerical model with symmetry boundary conditions imposed at the poles were found to be identical to the solutions from the other test. These findings indicate that the pole treatment does not induce unwanted, numerical artifacts into the solutions.

Numerical convergence studies were performed using the solution obtained from the finest discretization in space and time as the reference. By changing the values of grid spacing in the r, θ and ϕ directions, along with the time step the solutions were compared to the reference (finest) solution. The results reported here are with a $51 \times 51 \times 51$ grid and a time step ≤ 0.01 for the hemispherical solution (half range in θ). In the case of full 3D convection (full range in θ), the number of grid points in the θ directions were increased and at least a $51 \times 71 \times 51$ grid was used.

4.2 Numerical Results

In this section we present results for nonlinear three-dimensional convection with supercritical patterns investigated in the relevant parameters space starting from random initial conditions.

Validation of the 3D code

By turning off the calculations in the third dimension (ϕ), we first test the 3D model to see how it compares with the axisymmetric results. As seen in Figure 13a, the result compares well with the axisymmetric calculations (Figure 8b) for the same set of parameters. Also shown in Figure 13b is the velocity vector plot showing the direction of fluid motion in the shells, due to which there is a shift in the concentration C contours.

1 mm Shells

The critical curves for Re_{cr} shown in Figure 2 along with the axisymmetric results are used as a guide to describe the 3D solutions. By specifying an operating Reynolds number Re_{op}=2.0 we compute nonlinear 3D convection for this set of parameters which mimic the experiments. This value of Re_{op} is supercritical during early times

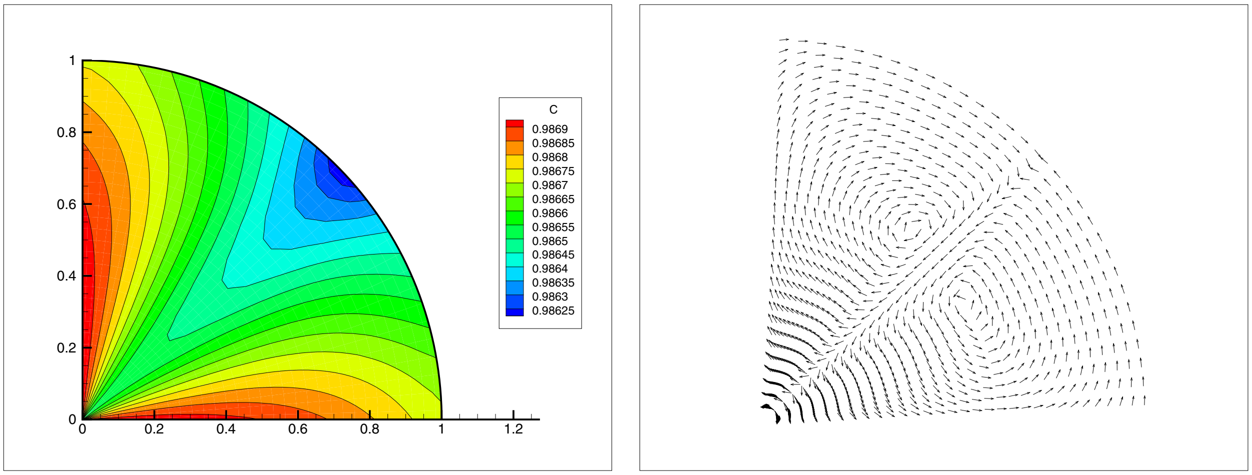

(a) (b)

Figure 13: Axisymmetric convection computed by the 3D code at the parameter values of Figure 8 (a) C contour plot (b) Velocity vector plot.

while is subcritical at later times. Thus we expect convection to first grow and then gradually weaken at later times. This is shown at early times in Figure 14. The motion with tetrahedral symmetry is very weak and the solution is almost axisymmetric. The iso-contours of concentration C in Figure 14b show that the motion is slowly developing in the latitudinal direction. A four cell motion ($l = 4$) which appears at a later time $t = 20.0$ is shown in Figure 15. As can be seen in the C contour plots in Figure 15 and 16, the contours are shifted in the direction of motion, with upwelling at the north and south poles. Also shown in Figure 16 are slice planes at two different values of θ and ϕ where we see an azimuthal wavenumber $m = 4$ motion in the ϕ direction. It is this $l = 4$ motion which persists over a long period of time during the curing process. At later times the motion dies down as a one cell motion when Re_{op} becomes subcritical. This is reasonable in comparison with the axisymmetric calculations where we found a three cell motion that exists for a long period of time and weakens as a one cell motion at later times. It should be noted that the computed cellular patterns are also in good agreement with the critical curves of Figure 2 which are flat up to modes 3-5 and the values of σ_{max} as computed from the linear theory. It is also noted that the computed convection with tetrahedral symmetry also exhibits hemispherical symmetry. In Figure 17, we find that in the case of hemispherical 3D convection, the motion at time $t = 30.0$ is once again the same four cell motion with tetrahedral symmetry and the C contours are shifted in the direction of motion as can be seen in the iso-contour plot in Figure 17b. The C contour plots at two slice planes in θ and ϕ are shown in Figure 18. It is also noted that the computed hemispherical solution exhibits tetrahedral symmetry.

Symmetry Comparison

Here we compute 3D convection in the entire sphere where $0 \leq \phi \leq 2\pi$. This is accomplished by imposing periodicity at $\phi = 2\pi$. As can be seen in Figure 19, we find that the 3D solution in this case is identical to the solution obtained with either of the symmetry conditions imposed (shown in Figures 15 and 17). Thus we conclude that 3D convection exhibits cubic symmetry.

2 mm Shells

The critical curves for Re_{cr} shown in Figure 9 along with the axisymmetric results are used as a guide to analyze the calculations. As in the case of axisymmetric convection, for $Re_{op} = 2.0$ which is supercritical at early times, multiple cell motions develop up to $t = 200.0$ as shown for the convection with tetrahedral symmetry in Figure 20. The

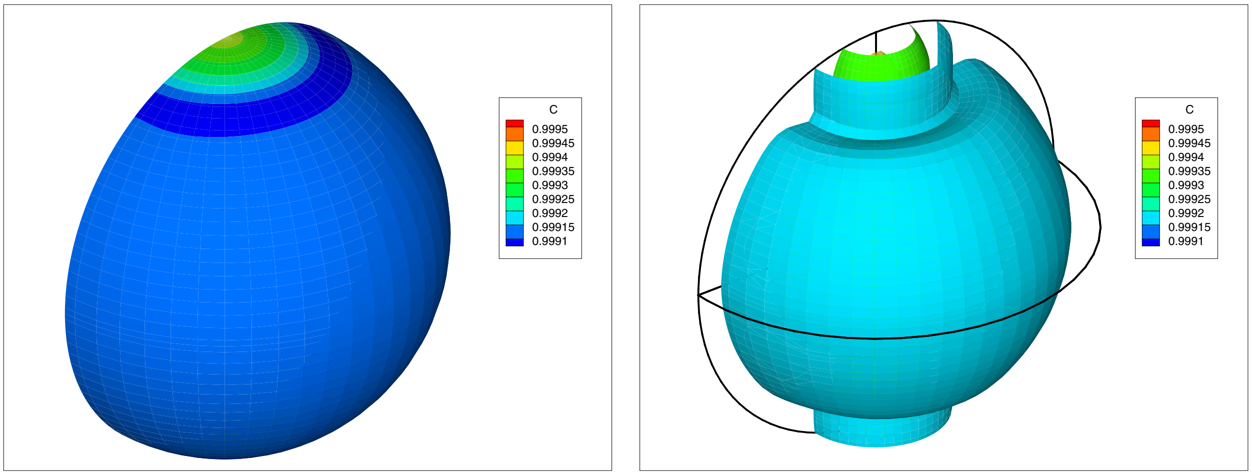

(a) (b)

Figure 14: 3D convection with tetrahedral symmetry in 1 mm shells at parameter values of Figure 2 at time $t = 1.0$ and Re_{op}=2.0. (a) Surface concentration C contour plot (b) Iso-contour levels.

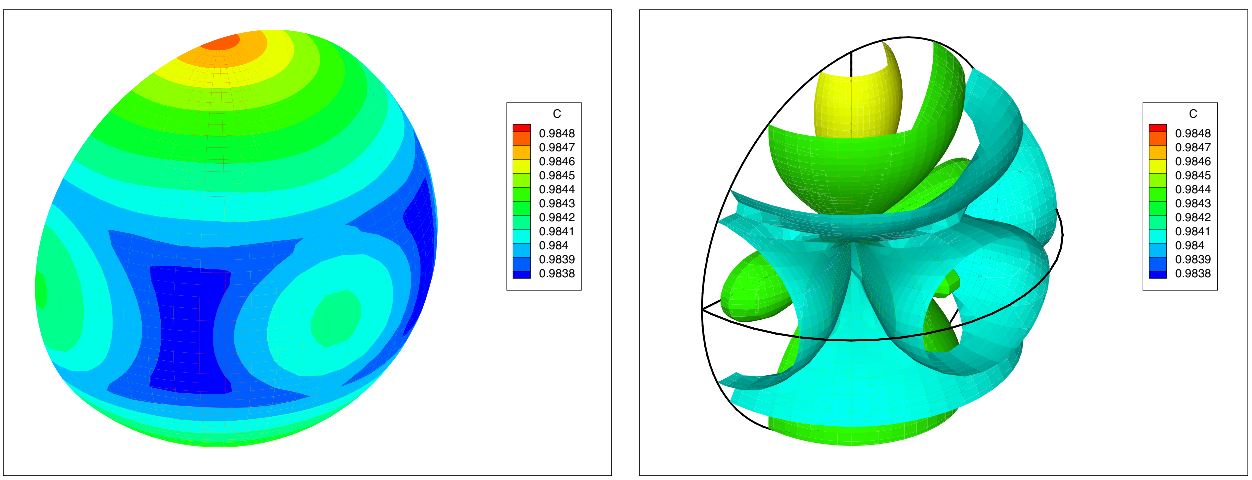

(a) (b)

Figure 15: Same as Figure 14 but at $t = 20.0$.

multiple cell motion which develops is not very clear in Figure 20a showing the contours on the surface which makes it seem almost axisymmetric. But this is not true, as can be seen from the $\phi = 0$ plane contour plots in Figure 21 where motions up to mode $l = 8$ develop in the 2 mm shells. The shifts in the contours of C in the direction of motion increase as time progresses. As a consequence of this, multiple modes in the azimuthal direction are also excited as can be seen in Figure 22. Due to the large values of l and m, the C contours in the equatorial plane ($\theta = 90$) possess a wavy nature which grows up to $t = 200.0$. At later times, as Re_{op} becomes subcritical, the shifts in C are minimal as the strength of the convection decreases until there is no further motion in the shell.

5 Surface Deformations

Equation (15) requires $\delta \sim O(Ca)$ in the limit $Ca \to 0$, so we write a perturbation series expansion for the surface deformation δ in terms of Ca

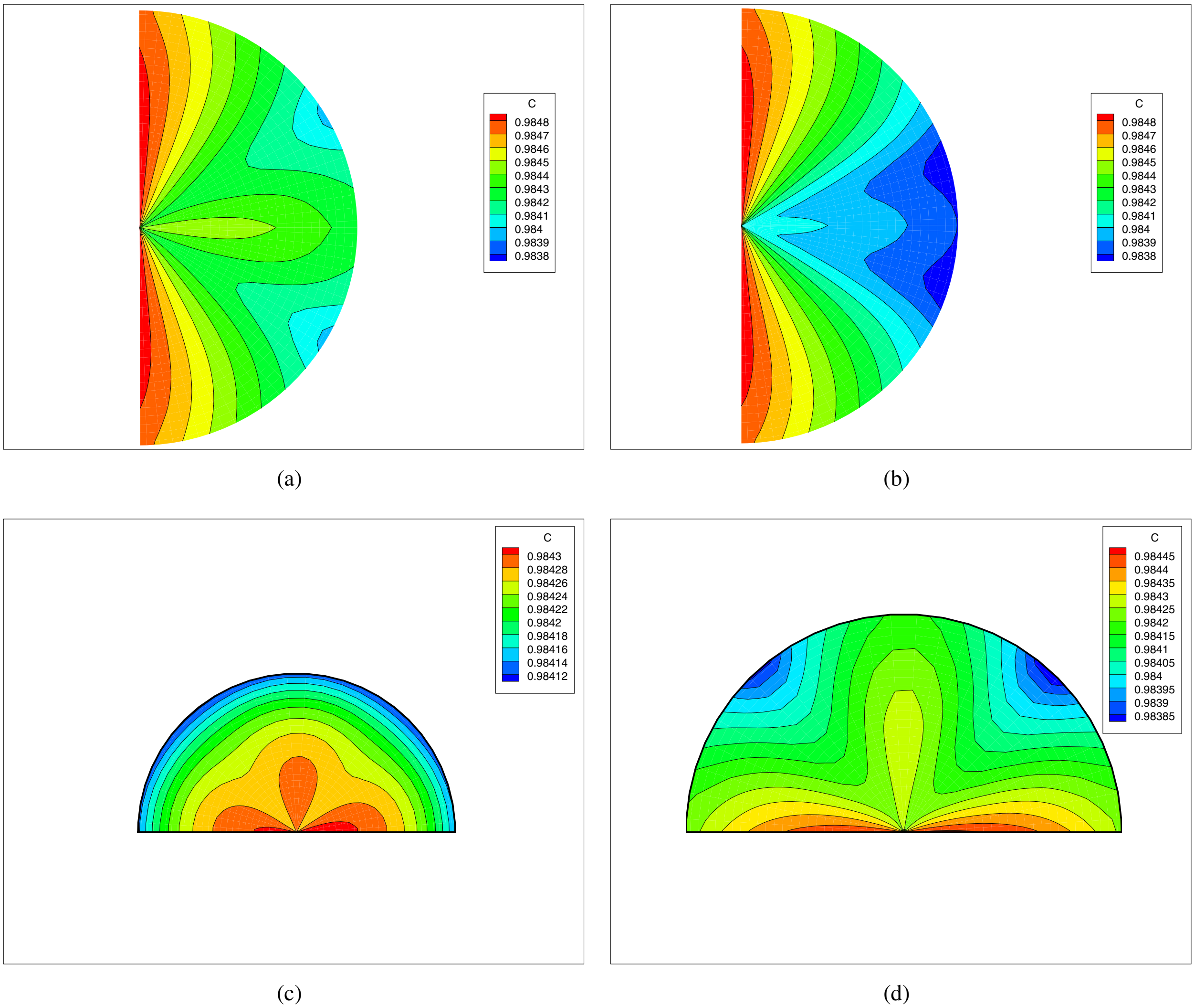

Figure 16: C contours at various slice planes corresponding to Figure 15 (a) $\phi = 0\,^\circ$ (b) $\phi = 45^\circ$ (c) $\theta = 45^\circ$ (d) $\theta = 90^\circ$.

as:

$$\delta = Ca\delta_1 + Ca^2\delta_2 + ..., \tag{20}$$

and we have:

$$[2 - L^2]\delta_1 = H(\theta, \phi, t) \tag{21}$$

where $H(\theta, \phi, t)$ is the l.h.s. of Eqn. (15) and represents the nonlinear convective motion arising from the fluid mechanics. The structure of Eqn. (21) demands careful analysis. If we consider the homogeneous form of Eqn. (21) i.e. with $H = 0$, then on re-arranging the terms we have:

$$[L^2]\delta_1 = 2\delta_1 \tag{22}$$

This equation is the eigenvalue problem of the L^2 operator, which has characteristic values $l(l+1)$ with corresponding analytic and 2π periodic eigenfunctions $Y_l^m(\theta, \phi)$ so that:

$$[L^2]Y_l^m = l(l+1)Y_l^m \tag{23}$$

where the surface harmonics (Chandrasekhar 1961) $Y_l^m = e^{im\phi}P_l^m(cos\theta)$, l is the latitudinal wavenumber (the degree of surface harmonic), and $|m| \leq l$ is the azimuthal wavenumber. From Eqn. (22) and Eqn. (23) we observe that the homogeneous problem for δ_1 has three nontrivial solutions with $l = 1$ given by Y_1^0, Y_1^1 and Y_1^{-1}. Hence the inhomogeneous

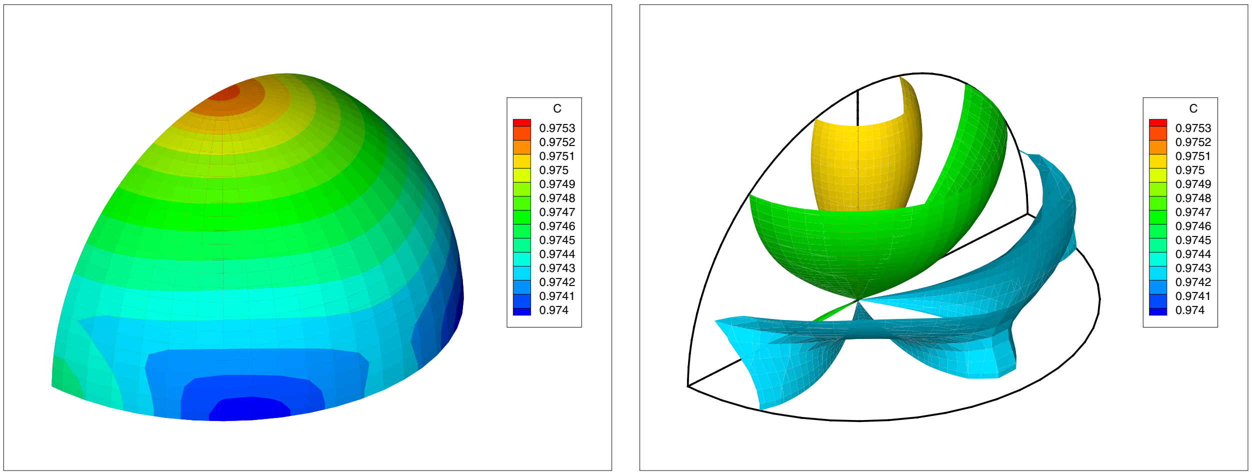

(a) (b)

Figure 17: 3D hemispherical convection in 1 mm shells at parameter values of Figure 2 at time $t = 30.0$ and Re_{op}=2.0. (a) Surface concentration C contour plot (b) Iso-contour levels.

problem in Eqn. (21) either has infinite number of solutions or no solutions depending on whether or not H is orthogonal to each of the nontrivial homogeneous solutions (Fredholm alternative theorem).

5.1 Compatibility of Axisymmetric Solutions

Here Eqn. (21) becomes:

$$\delta_{1,\theta\theta} + cot\theta\delta_{1,\theta} + 2\delta_1 = H(\theta,t), \tag{24}$$

and there is only one nontrivial homogeneous solution $Y_1^0 = cos\theta$. It is shown (see Appendix B) that compatibility requires H to be orthogonal to $x = cos\theta$ in $0 < \theta < \pi$ so that:

$$\int_{x=-1}^{+1} Hxdx = 0 \tag{25}$$

which implies that H has to be symmetric about $x = 0$ (or $\theta = \pi/2$). Thus only the solutions with hemispherical symmetry are compatible in the axisymmetric case.

5.2 Compatibility of 3-D Solutions

In 3-D, the δ_1 equation is given by:

$$\delta_{1,\theta\theta} + cot\theta\delta_{1,\theta} + \frac{1}{sin^2\theta}\delta_{1,\phi\phi} + 2\delta_1 = H(\theta,\phi,t), \tag{26}$$

and we have three nontrivial homogeneous solutions $Y_1^0 = cos\theta$ and $Y_1^{\pm 1} = sin\theta e^{i\phi}$ ($sin\theta sin\phi$ and $sin\theta cos\phi$). As in the case of axisymmetry we can show (see Appendix C) that the only compatible H must satisfy the following orthogonality relations in $0 < \theta < \pi$ and $0 < \phi < 2\pi$:

$$\int_{\phi=0}^{2\pi}\int_{x=-1}^{+1} Hxdxd\phi = 0 \tag{27}$$

$$\int_{\phi=0}^{2\pi}\int_{x=-1}^{+1} H\sqrt{1-x^2}e^{i\phi}dxd\phi = 0 \tag{28}$$

Thus only the solutions with cubic symmetry are admissible.

5.3 The Global Conservation Condition

We rewrite Eqn. (21) as

$$[2 - L^2]\delta_1 = h(\theta,\phi,t) + \alpha(t) \tag{29}$$

where $H(\theta,\phi,t) = h(\theta,\phi,t) + \alpha(t)$ and $\alpha(t)$ is an arbitrary function of time associated with the pressure field and also contains the capillary pressure term $2r_{2d}/Ca$. The solution to Eqn. (29) is written as:

$$\delta_1 = \delta_{1p} + \alpha(t)\delta_{1g} \tag{30}$$

where $[2 - L^2]\delta_{1g} = 1$ and $[2 - L^2]\delta_{1p} = h(\theta,\phi,t)$.

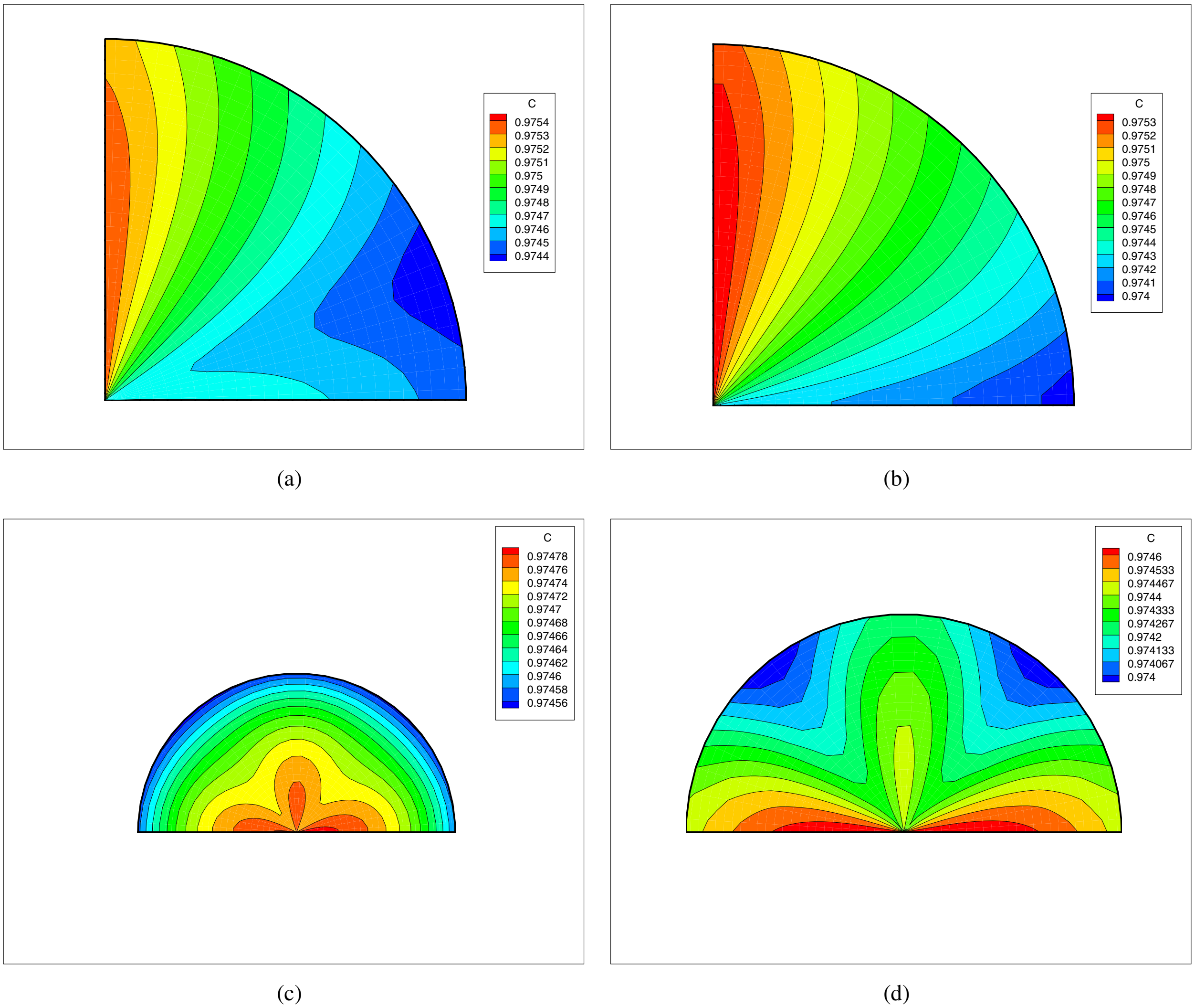

Figure 18: C contours at various slice planes corresponding to Figure 17 (a) $\phi = 0\,°$ (b) $\phi = 45°$ (c) $\theta = 45°$ (d) $\theta = 90°$.

We now need a global conservation condition on δ_1 in order to determine $\alpha(t)$. This may be obtained by equating the swept volume of solvent shown in Figure 23 and given by:

$$\int_\Omega \int_{R_2}^{R_{20}} r^2 dr d\Omega \tag{31}$$

to the evaporated volume resulting from the convection-diffusion process and given by:

$$\int_0^t \int_a \dot{m}'' dadt = \int_0^t \int_a (\underline{u} - \underline{v}) \cdot \hat{n} dadt \tag{32}$$

where $\dot{m}''$ is the solvent mass flux and $R_2(\theta,\phi,t) = r_{2d}(t) + Ca\delta_1(\theta,\phi,t) + O(Ca^2)$. From Figure 24 we have $da = R_2^2 N d\Omega$, it was shown (Subramanian et al 2005a; Subramanian 2005) that $\underline{v} \cdot \hat{n} = (-1/|\nabla F|)(\partial F/\partial t) = \dot{R}_2/N$, and $\nabla \cdot \underline{u} = 0$ requires $\int_a (\underline{u} \cdot \hat{n}) da = 0$. Hence we find that the expressions for the amount of mass transfer m_v is identically given by either Eqns. (31) or (32), i.e. we have the identity:

$$\int_\Omega \int_{R_2}^{R_{20}} r^2 dr d\Omega \equiv -\int_0^t \int_\Omega R_2^2 \dot{R}_2 d\Omega dt \tag{33}$$

Thus the net mass transfer m_v is calculated by either of the integrals in Eqn. (33) as:

$$m_v = \int_\Omega \frac{1}{3}[R_{2_0}^3 - R_2^3] d\Omega, \tag{34}$$

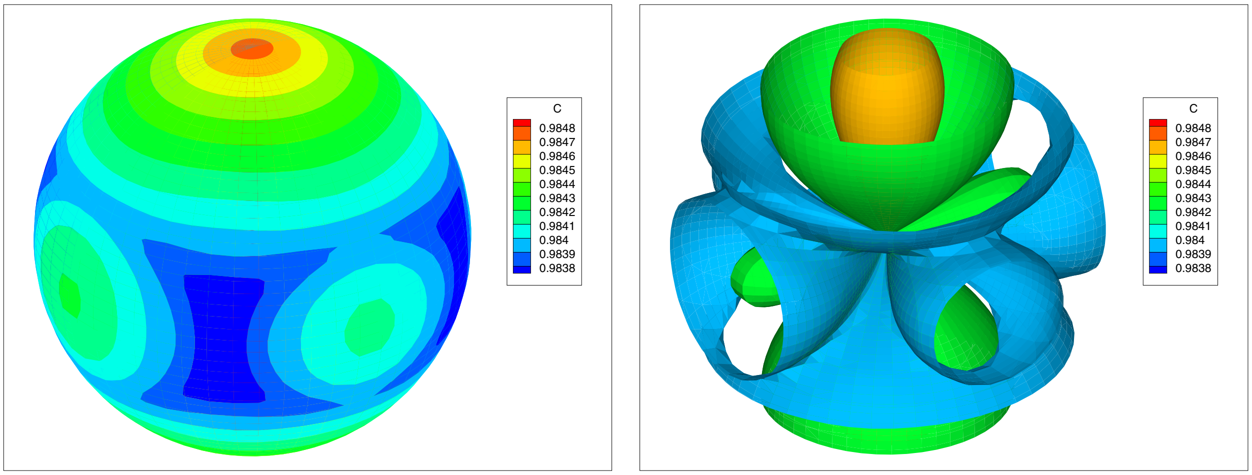

(a) (b)

Figure 19: 3D full sphere convection in 1 mm shells with periodic boundary conditions in ϕ (corresponding to Figures 15 and 17).

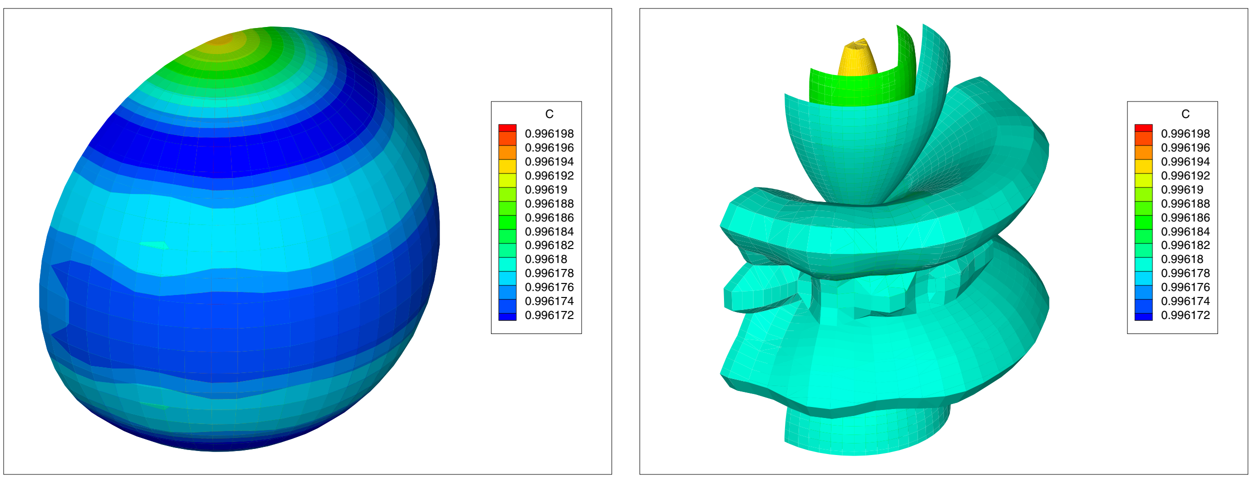

(a) (b)

Figure 20: 3D convection in 2 mm shells at parameter values of Figure 9 at time $t = 200.0$ and Re_{op}=2.0. (a) Surface concentration C contour plot (b) Iso-contour levels.

and is further given by:

$$m_v = \frac{4}{3}\pi[R_{2_0}^3 - r_{2d}^3] - Ca\int_\Omega r_{2d}^2\delta_1 d\Omega - O(Ca^2) \tag{35}$$

Had there been no mass transfer, i.e. $m_v = 0$ and $R_{2_0} = r_{2d} = constant$, Eqn. (35) would provide the required global conservation condition to calculate $\alpha(t)$. Note that m_v also represents the net mass transfer across the interface due to convection and diffusion. The first term in the right-hand side of Eqn. (35) represents the mass transfer purely by diffusion given by $m_d = \frac{4}{3}\pi[R_{2_0}^3 - r_{2d}^3]$. If it is reasonable to assume $m_v \geq m_d$ then we must have:

$$\int_\Omega \delta_1(\theta,\phi,t)d\Omega \leq 0, \tag{36}$$

and with δ_1 given by Eqn. (30), we have:

$$\int_\Omega \delta_{1p} d\Omega + \alpha(t)\int_\Omega \delta_{1g} d\Omega \leq 0 \tag{37}$$

This inequality can be used to calculate an upper bound for δ_1 in the following way. Be-

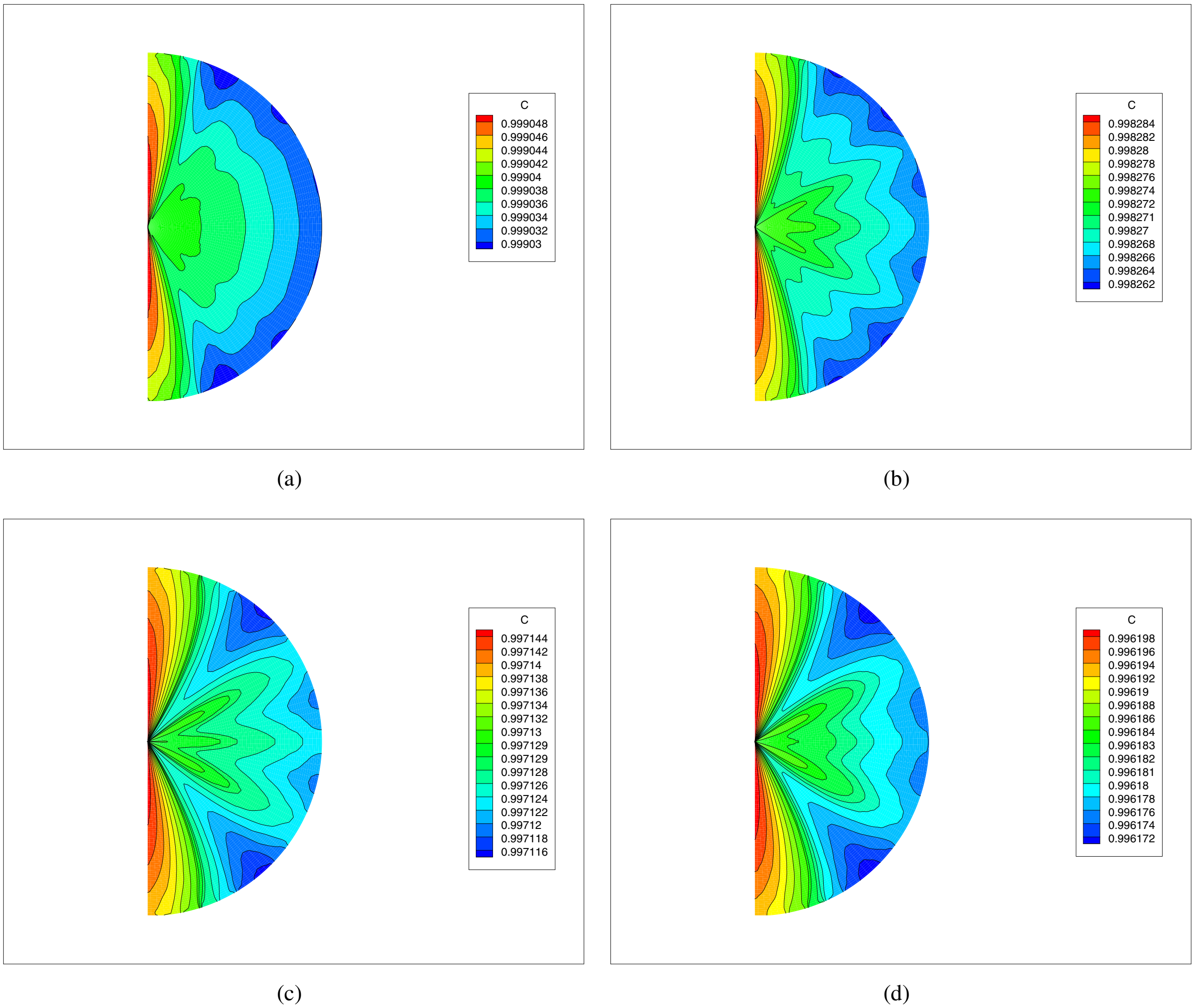

Figure 21: C contours in 2 mm shells at various times t and Re_{op}=2.0 along the plane at $\phi = 0^\circ$ (a) $t = 50.0$ (b) $t = 100.0$ (c) $t = 150.0$ (d) $t = 200.0$.

cause $\delta_{1g} > 0$ and $\int_\Omega \delta_{1g} d\Omega > 0$, we have $\alpha(t) \leq -\frac{\int_\Omega \delta_{1p} d\Omega}{\int_\Omega \delta_{1g} d\Omega}$. Since $\int_\Omega \delta_{1p} d\Omega$ was found < 0 choosing the equality determines the deflection with the largest positive δ_1.

5.4 Numerical Scheme

We write expansions for δ_1 and H in terms of surface harmonics (Chandrasekhar 1961) as $\delta_1 = \sum_{l=0}^{\infty} \sum_{m=-l}^{+l} \delta_{1lm} e^{im\phi} P_l^m$, $H = \sum_{l=0}^{\infty} \sum_{m=-l}^{+l} H_{lm} e^{im\phi} P_l^m$ so that Eqn. (21) becomes:

$$\sum_{l=0}^{\infty} \sum_{m=-l}^{+l} [2 - l(l+1)] \delta_{1lm} e^{im\phi} P_l^m$$

$$= \sum_{l=0}^{\infty} \sum_{m=-l}^{+l} H_{lm} e^{im\phi} P_l^m \quad (38)$$

or $\delta_{1lm} = H_{lm}/[2 - l(l+1)] \implies$ we clearly have a problem when $l = 1$ except if $H_{1m} = 0$ which is precisely the compatibility condition. According to Eqn. (29) we also write $H_{lm} = h_{lm} + \alpha_{lm}$ where $\alpha_{lm} = \alpha(t)$ if $l = m = 0$ and zero otherwise. Hence we have:

$$[2 - l(l+1)] \delta_{1lm} = (h_{00} + \alpha) + h_{lm} \quad (39)$$

for all $l \geq 1$ and $|m| \leq l$. It is important to observe that if h does not contain Y_1^0 and $Y_1^{\pm 1}$ then it is compatible. This is only true for the cubic solutions in 3D and the hemispherical solutions in 2D

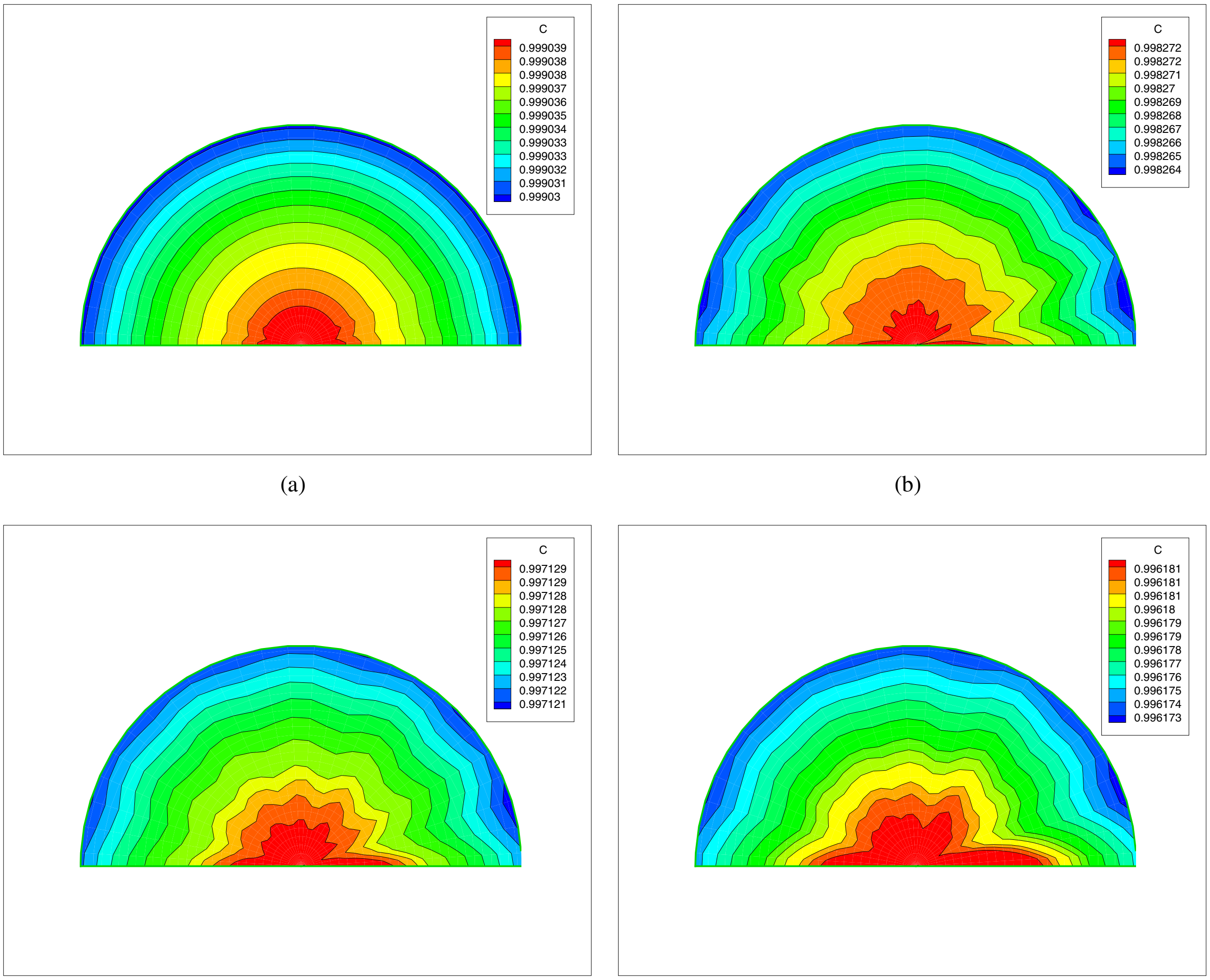

(a) (b)

(c) (d)

Figure 22: C contours in 2 mm shells at various times t and Re_{op}=2.0 along the plane at $\theta = 90^\circ$ (a) $t = 50.0$ (b) $t = 100.0$ (c) $t = 150.0$ (d) $t = 200.0$.

($m = 0$) in which case we have:

$$\delta_1 = \frac{(h_{00}+\alpha)}{2} + \sum_{l=2}^{\infty}\sum_{m=-l}^{+l} \frac{h_{lm}}{2-l(l+1)} e^{im\phi} P_l^m \tag{40}$$

5.5 Numerical Results

In this section, we present the admissible axisymmetric and 3D solutions for maximum δ_1 at parameter values close to those in the experiments with the 1 and 2 mm shells. Figure 25 shows the axisymmetric maximum δ_1 at $t = 10.0$ in 1 mm shells. Also shown in Figure 25 are the individual contributions to maximum δ_1 from the pressure, concentration and viscous terms in the normal stress balance Eqn. (15). The variation of maximum δ_1 with time for the 1 and 2 mm shells is shown in Figure 26 where its magnitude increases as the motion develops and Re_{op} is supercritical. At later times when the motion is weak and Re_{op} is subcritical there is no further change in maximum δ_1.

As seen in Figure 27, the 3D maximum δ_1 in the 1 mm shells is almost axisymmetric at early times. This is reasonable as the motion is only developing at early times when Re_{op} is supercritical. Figure 28 shows that at later times ($t = 20.0$), the maximum δ_1 has a more three-dimensional struc-

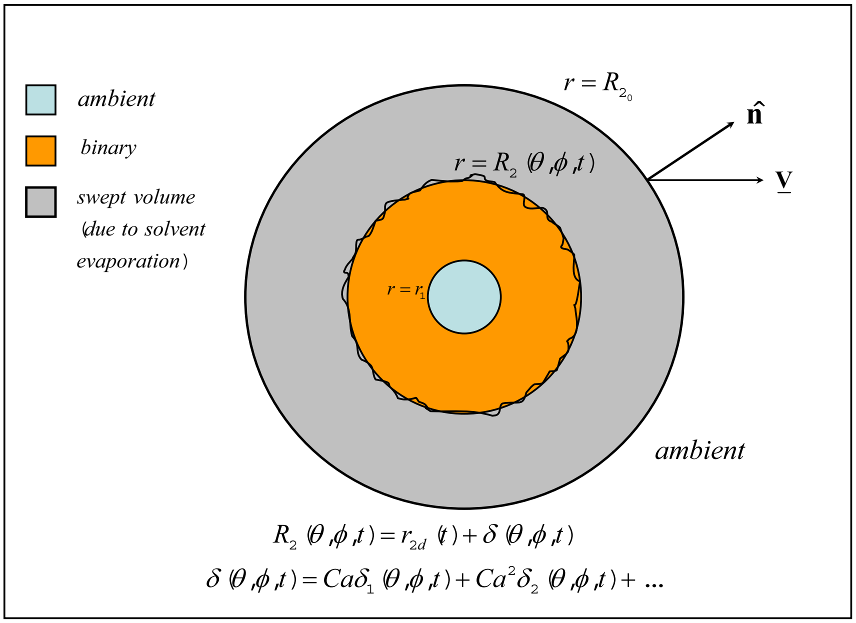

Figure 23: Swept volume of solvent during evaporation

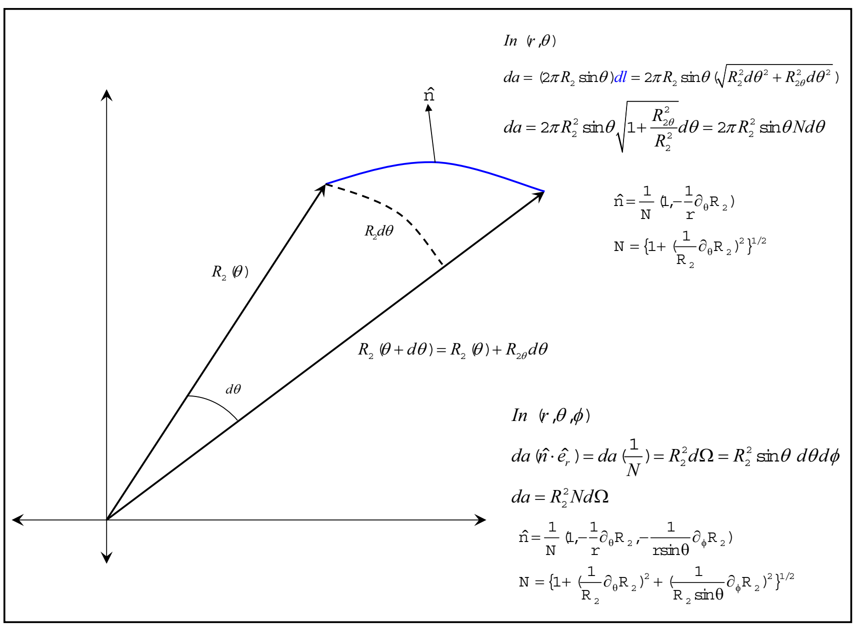

Figure 24: Differential geometry of the moving interface

ture. This is consistent with the $l = 4$, $m = 4$ motion which develops in the shells at this t (see Figure 15). The maximum value of δ_1 in the 1 mm shells is order 0.01 and hence the actual maximum physical value of δ^* computed is order $1 \cdot Ca$ microns (i.e. $\delta^* = \delta_1 * L_r * Ca$, where L_r=0.122 mm).

The value of maximum δ_1 at $t = 100.0$ in the 2 mm shells is shown in Figure 29. At a later time $t = 200.0$ the surface deflection has a more

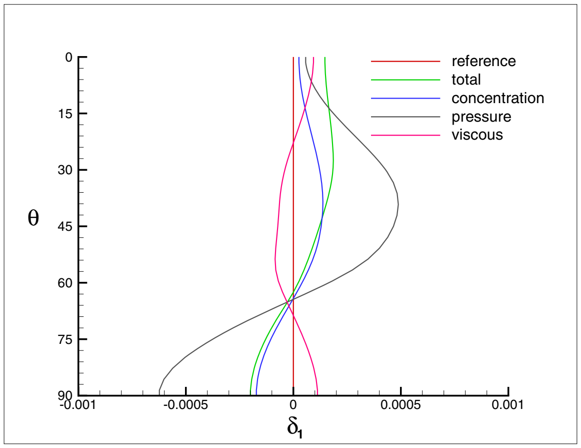

Figure 25: Axisymmetric maximum surface deflection δ_1 at time $t = 10.0$ and Re_{op}=2.0 for the 1 mm shells at parameter values of Figure 2.

involved structure as can be seen in Figure 30. As the maximum value of δ_1 is about 0.04-0.05, the actual maximum physical value of δ^* computed for the 2 mm shells is order $3 \cdot Ca$ microns (where L_r=0.077 mm). This is in reasonable comparison with experiments (McQuillan et al 2004) where the maximum magnitude of the surface deflections for the 2 mm shells is about 1 micron.

6 Concluding Remarks

We have developed a mathematical model for solutocapillary instabilities in spherical shells. The outer surface of the shell recedes due to mass transfer of the solvent into the ambient. To leading order in the limit $(Ca \rightarrow 0)$ $r_2(t)$ is fixed by the nonlinear system that describes the diffusive state (Subramanian et al 2005a; Subramanian 2005). Linear instability of this time-dependent diffusive state was determined from frozen time or quasi-steady state analysis and from time evolving initial value problem calculations. (Subramanian et al 2005a) Results from these two approaches are in agreement for $t > 0$ with dependence on initial conditions only near $t = 0$. The results for the diffusive state solution and linear stability analysis are also in good qualitative and quantitative agreement with the experiments (Subramanian et al 2005a; Subramanian 2005).

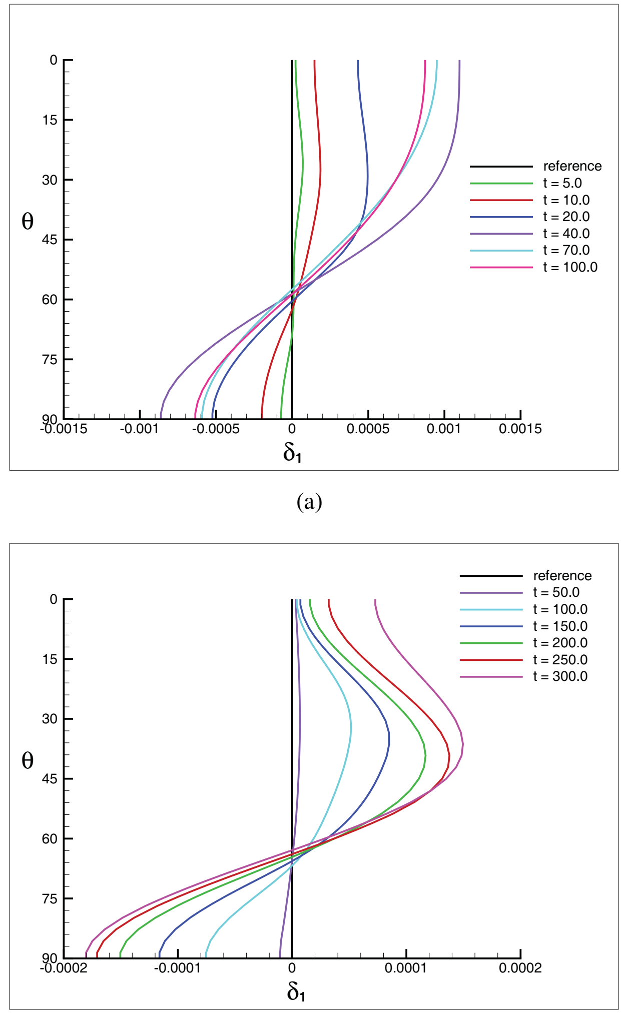

(a)

(b)

Figure 26: Axisymmetric maximum surface deflection δ_1 at various times t and Re_{op}=2.0 (a) 1 mm shells at parameter values of Figure 2. (b) 2 mm shells at parameter values of Figure 9.

The linear system is degenerate and is independent of the azimuthal wavenumber. A nonlinear selection mechanism is expected which also determines the convective amplitude and hence δ. Time-dependent, nonlinear, variable viscosity, axisymmetric and three-dimensional studies were performed to calculate the supercritical motions and associated compatible dynamic free surface deformations. It was shown that the only possible 3D motion possesses cubic symmetry. The results from the nonlinear computations compare well with linear theory.

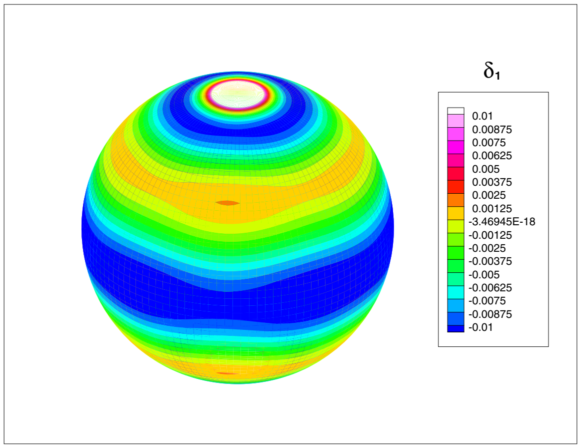

Figure 27: Contours of 3D maximum surface deflection δ_1 for 1 mm shells at time $t = 5.0$ and Re_{op}=2.0 at parameter values of Figure 2.

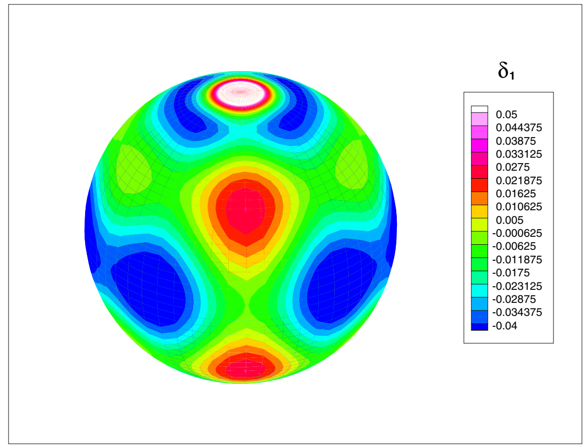

Figure 29: Contours of 3D maximum surface deflection δ_1 for 2 mm shells at time $t = 100.0$ and Re_{op}=2.0 at parameter values of Figure 9.

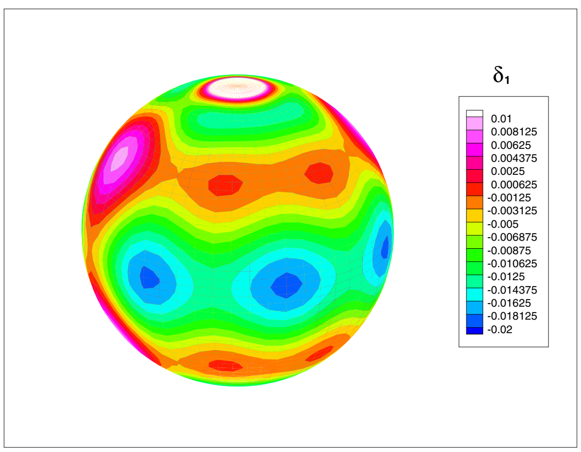

Figure 28: Contours of 3D maximum surface deflection δ_1 for 1 mm shells at time $t = 20.0$ and Re_{op}=2.0 at parameter values of Figure 2.

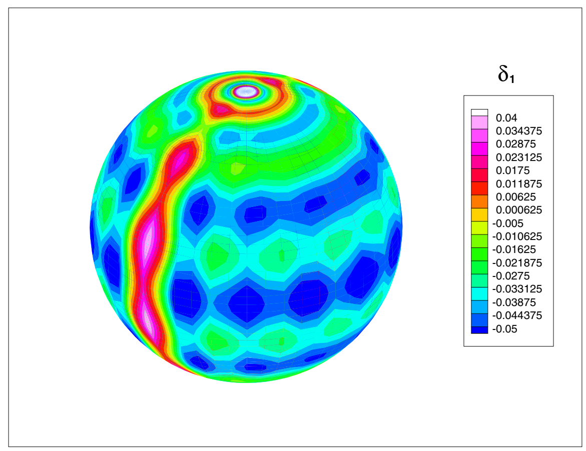

Figure 30: Contours of 3D maximum surface deflection δ_1 for 2 mm shells at time $t = 200.0$ and Re_{op}=2.0 at parameter values of Figure 9.

Our mathematical model is applicable to the drying phase of microencapsulation of ICF targets. Comparisons between our theoretical predictions and measurements indicate good agreement given the uncertainty in the values of thermodynamic properties and conditions in the experiments. Hence, we conclude that the Marangoni instabilities could well be the source of the observed surface roughness in the shells.

Acknowledgement: We gratefully acknowledge support of the National Science Foundation (NSF Grant # CTS-0211612) and the Rutgers University Engineering Computing Services.

APPENDIX A

The dimensionless normal stress balance at the outer interface is given by:

$$\hat{n} \cdot S \cdot \hat{n} = -\frac{Ma}{Ca}(1 - CaC)\nabla \cdot \hat{n} \tag{A1}$$

Substituting $R_2(\theta,\phi,t) = r_2(t) + \delta(\theta,\phi,t)$ in Eqn. (14) we have:

$$\hat{n} = (1, -\frac{1}{r}\partial_\theta \delta, -\frac{1}{r sin\theta}\partial_\phi \delta) + O(\delta^2) \quad \text{(A2)}$$

and

$$\nabla \cdot \hat{n} = \big[\frac{1}{r^2}\frac{\partial(r^2)}{\partial r} - \frac{1}{r^2 sin\theta}\frac{\partial}{\partial\theta}(sin\theta\frac{\partial\delta}{\partial\theta}) - \frac{1}{r^2 sin^2\theta}\frac{\partial^2\delta}{\partial\phi^2}\big] + O(\delta^2) \quad \text{(A3)}$$

Hence (A1) reduces to:

$$-p + 2\mu\frac{\partial u_r}{\partial r} = -\frac{Ma}{Ca}(1-CaC)\big[\frac{2}{r} + \frac{L^2}{r^2}(\delta)\big] + O(\delta^2) \quad \text{(A4)}$$

Writing $r = r_2 + \delta$ we have to $O(\delta)$ at $r = r_2$:

$$-p + 2\mu\frac{\partial u_r}{\partial r} = -\frac{2Ma}{r_2 Ca} + \frac{2MaC}{r_2} + \frac{Ma}{{r_2}^2}[2-L^2](\frac{\delta}{Ca}) + O(\delta) \quad \text{(A5)}$$

which on rearrangement gives Eqn (15).

APPENDIX B

In axisymmetry, we begin with the equation for $\delta_1(\theta,t)$:

$$(2-L^2)[\delta_1] = \delta_{1,\theta\theta} + cot\theta\,\delta_{1,\theta} + 2\delta_1 = H(\theta,t) \quad \text{(B1)}$$

Substituting $x = cos\theta$, we have $\delta_{1,\theta} = -\delta_{1,x} sin\theta$ and $\delta_{1,\theta\theta} = \delta_{1,xx} sin^2\theta - \delta_{1,x} cos\theta$. Thus Eqn. (B1) is re-written as:

$$(1-x^2)\delta_{1,xx} - 2x\delta_{1,x} + 2\delta_1 = [(1-x^2)\delta_{1,x}]_x + 2\delta_1 = H(x,t) \quad \text{(B2)}$$

We now have:

$$\int_{x=-1}^{+1} xH dx = \int_{x=-1}^{+1} \Big([(1-x^2)\delta_{1,x}]_x + 2\delta_1\Big) x dx \quad \text{(B3)}$$

which reduces to:

$$[(1-x^2)\delta_{1,x}]x\Big|_{-1}^{1} - (1-x^2)\delta_1\Big|_{-1}^{1} - \int_{x=-1}^{+1} 2\delta_1 x dx + \int_{x=-1}^{+1} 2\delta_1 x dx = 0 \quad \text{(B4)}$$

APPENDIX C

In three dimensions, we begin with the equation for $\delta_1(\theta,\phi,t)$:

$$\delta_{1,\theta\theta} + cot\theta\,\delta_{1,\theta} + \frac{1}{sin^2\theta}\delta_{1,\phi\phi} + 2\delta_1 = H(\theta,\phi,t) \quad \text{(C1)}$$

Substituting $x = cos\theta$ this becomes:

$$[(1-x^2)\delta_{1,x}]_x + \frac{1}{(1-x^2)}\delta_{1,\phi\phi} + 2\delta_1 = H(x,\phi,t) \quad \text{(C2)}$$

Now we have:

$$\int_{\phi=0}^{2\pi}\int_{x=-1}^{+1} xH dx d\phi = \int_{\phi=0}^{2\pi}\int_{x=-1}^{+1} \Big([(1-x^2)\delta_{1,x}]_x + \frac{1}{(1-x^2)}\delta_{1,\phi\phi} + 2\delta_1\Big) x dx d\phi \quad \text{(C3)}$$

which can be re-written as:

$$\int_{\phi=0}^{2\pi}\Big[\int_{x=-1}^{+1}\Big([(1-x^2)\delta_{1,x}]_x + 2\delta_1\Big) x dx\Big] d\phi + \int_{\phi=0}^{2\pi}\Big[\int_{x=-1}^{+1}\frac{x}{(1-x^2)}dx\Big]\delta_{1,\phi\phi} d\phi \quad \text{(C4)}$$

Noting that the integral in (B3) vanishes, (C4) reduces to:

$$\int_{\phi=0}^{2\pi}\delta_{1,\phi\phi} d\phi \int_{x=-1}^{+1}\frac{x}{(1-x^2)}dx \quad \text{(C5)}$$

which is identically zero if δ_1 is a single valued function of ϕ. Thus the r.h.s. of (C3) is zero. We also have:

$$\int_{\phi=0}^{2\pi}\int_{x=-1}^{+1} xH\sqrt{1-x^2}e^{i\phi} dx d\phi = \int_{\phi=0}^{2\pi}\int_{x=-1}^{+1}\Big([(1-x^2)\delta_{1,x}]_x + \frac{1}{(1-x^2)}\delta_{1,\phi\phi} + 2\delta_1\Big)\sqrt{1-x^2}e^{i\phi} dx d\phi \quad \text{(C6)}$$

Noting that:

$$\int_{x=-1}^{+1}\Big([(1-x^2)\delta_{1,x}]_x\Big)\sqrt{1-x^2}dx =$$

$$-\int_{x=-1}^{+1} \delta_1 \sqrt{1-x^2}dx + \int_{x=-1}^{+1} \delta_1 \frac{x^2}{\sqrt{1-x^2}}dx \tag{C7}$$

We have that (C6) reduces to:

$$\int_{\phi=0}^{2\pi}\int_{x=-1}^{+1} \Big(\delta_1 \sqrt{1-x^2} + \delta_1 \frac{x^2}{\sqrt{1-x^2}} + \frac{\delta_{1,\phi\phi}}{\sqrt{(1-x^2)}}\Big) e^{i\phi}\, dx d\phi \tag{C8}$$

which can be re-written as:

$$\int_{\phi=0}^{2\pi}\int_{x=-1}^{+1} \frac{(\delta_1 + \delta_{1,\phi\phi})}{\sqrt{(1-x^2)}} e^{i\phi} dx d\phi \tag{C9}$$

Now:

$$\begin{aligned}&\int_{\phi=0}^{2\pi} (\delta_1 + \delta_{1,\phi\phi}) e^{i\phi} d\phi = \\ &\int_{\phi=0}^{2\pi} \delta_1 e^{i\phi} d\phi + (\delta_{1,\phi} e^{i\phi}\Big|_0^{2\pi}) \\ &-\Big[\delta_1 i e^{i\phi}\Big|_0^{2\pi} - \int_{\phi=0}^{2\pi} \delta_1 i^2 e^{i\phi} d\phi\Big] \\ &= 0\end{aligned} \tag{C10}$$

Hence it follows that (C9) is also identically zero and the r.h.s. of (C6) is zero.

References

Chandrasekhar, S. (1961): *Hydrodynamic and Hydromagnetic Stability*, Oxford University Press, New York.

Cloot, A.; Lebon, G. (1985): Marangoni Instability in a Fluid Layer with Variable Viscosity and Free Interface in Microgravity, *PCH PhysicoChemical Hydrodynamics*, **6**, 453.

Hoefsloot, H. C. J.; Hoogstraten, H. W.; Janssen, L. P. B. M. (1990): Marangoni Instability in a Liquid Layer Confined Between Two Concentric Spherical Surfaces Under Zero-gravity Conditions, *Appl. Sci. Res.*, **47**, 357.

McQuillan, B. W. (1997): The PAMS/GDP Process for Production of ICF Target Mandrels, *Fusion Technol.*, **31**, 381.

McQuillan, B. W.; Greenwood, A. (1999): Microencapsulation Process Factors which Influence Sphericity of 1 mm O.D. Poly (α-methyl styrene) Shells for ICF, *Fusion Technol.*, **35**, 194-197.

McQuillan, B.; Paguio, R.; Subramanian, P.; Takagi, M.; Zebib, A. (2004): Hydrodynamic Issues in PAMS Mandrel Target Fabrication, *Proceedings of the 3rd International Conference on Inertial Fusion Sciences and Applications*, American Nuclear Society, 766-769.

McQuillan, B. W.; Takagi, M. (2002): Removal of Mode 10 Surface Ripples in ICF PAMS Shells, *Fusion Science and Technology*, **41**, 209-213.

Patankar, S. V. (1980): *Numerical Heat Transfer and Fluid Flow*, Series in Computational Methods in Mechanics and Thermal Sciences, Hemisphere, Washington DC.

Pearson, J. R. A. (1958): On Convection Cells Induced by Surface Tension, *J. Fluid Mech.*, **4**, 489.

Smith, K. A. (1966): On Convective Instability Induced by Surface Tension Gradients, *J. Fluid Mech.*, **24**, 401.

Subramanian, P. (2005): *Theoretical and Computational Study of Solutocapillary Spherical Convection in Microencapsulation*, Ph.D. Dissertation, Department of Mechanical and Aerospace Engineering, Rutgers, The State University, New Jersey.

Subramanian, P.; Zebib, A.; McQuillan, B. (2005a): Solutocapillary Convection in Spherical Shells, *Physics of Fluids*, **17**, 1-10.

Subramanian, P.; Zebib, A.; McQuillan, B. (2005b): Axisymmetric Marangoni Convection in Microencapsulation, *Acta Astronautica*, **57**, 97-103.

Wilson, S. K. (1994): The Onset of Steady Marangoni Convection in a Spherical Geometry, *J. Eng. Math.*, **28**, 427.